Oblique shock control with steady flexible panels

Journal:	*AIAA Journal*
Manuscript ID	2019-08-J058933.R1
Manuscript Type:	Regular Article
Date Submitted by the Author:	n/a
Complete List of Authors:	Gomez-Vega, Nicolas; Imperial College London, Aeronautics Gramola, Michela; Imperial College London, Aeronautics Bruce, Paul; Imperial College London, Aeronautics
Subject Index Category:	21500 Shock Waves and Detonations < 20000 FLUID DYNAMICS, 21700 Supersonic Flow < 20000 FLUID DYNAMICS, 01210 Flow Control < 00000 AIRCRAFT TECHNOLOGY, CONVENTIONAL, STOL/VTOL
Select ONE Subject Index for the Table of Contents. This is where your paper will show up in the Table of Contents:	20000 FLUID DYNAMICS
Note: The following files were submitted by the author along with the article. You may review these files online, if you wish. Acceptance for publication will be based solely on the content of the article.	
source.zip	

Oblique shock control with steady flexible panels

Nicolas Gomez-Vega*, Michela Gramola†, and Paul J. K. Bruce‡
Department of Aeronautics, Imperial College London, SW7 2AZ, United Kingdom

Flexible panels deforming under pressure loads have been suggested as a passive form of adaptive oblique shock control. This study investigates oblique shock–boundary layer interactions on a steady flexible panel in a Mach 2.0 flow. Experiments were performed in the Imperial College supersonic wind tunnel, where shock generators were used to produce an oblique shock followed by a corner expansion. A parametric study was conducted, exploring different shock impingement positions and shock–expansion distances. The steady aero-structural response is studied using schlieren photography, static pressure distributions, photogrammetry measurements, and surface oil flow visualisation. Two-dimensional numerical simulations were performed to assess the effects of the flexible panel on downstream total pressure recovery. These were validated against experimental wall pressure distributions and measurements from a Pitot rake. Results show reductions in both separation length (of up to 40 %) and stagnation pressure losses (of up to 10 %) if the flexible plate is used. These improvements occur for a range of shock positions spanning approximately 50 % of the panel length and for all the shock–expansion distances considered. A model that captures the flow physics responsible for these trends is proposed. The results highlight the potential of flexible panels for practical oblique shock control.

Nomenclature

a	=	plate length, mm
$\mathcal{AR}$	=	tunnel aspect ratio
c_f	=	skin-friction coefficient
l	=	mesh target surface size, mm
L_{int}	=	interaction length, mm
L_{sep}	=	separation length, mm
P_a	=	atmospheric pressure, Pa
P_c	=	cavity pressure, Pa

*Graduate, Department of Aeronautics, Imperial College London
†PhD Candidate, Department of Aeronautics, Imperial College London, AIAA Student Member
‡Senior Lecturer, Department of Aeronautics, Imperial College London, AIAA Senior Member

P_p = Pitot pressure, Pa

P_0 = stagnation pressure, Pa

$P_{0,s}$ = settling chamber stagnation pressure, Pa

t_{SG} = shock generator thickness, mm

u = flow velocity, m s^{-1}

w = plate deflection, mm

x_e = impingement point of the expansion's head, mm

x_r = re-attachment point, mm

x_s = separation point, mm

x_{SG} = shock generator streamwise location, mm

x_1 = inviscid shock impingement point, mm

y^+ = dimensionless wall distance

δ = boundary layer thickness, mm

θ = flow deflection, deg

ρ = density, kg m^{-3}

I. Introduction

The main function of a supersonic engine inlet is to decelerate the flow to subsonic conditions in the most efficient way possible, without great losses in stagnation pressure. A common strategy for this involves the generation of oblique shock structures, reflecting off the internal surfaces of the inlet. As these shocks meet the boundary layers growing along the surfaces, shock–boundary layer interactions (SBLIs) develop. These often cause undesirable separation and unsteadiness, leading to stagnation pressure losses and lower efficiency. Therefore, it is not surprising that oblique SBLIs have become a target for flow control [1–6].

A promising method for SBLI control are shock control bumps, which are contoured protrusions on aerodynamic surfaces. These have been investigated for applications ranging from transonic wings [7–9] to engine inlets [3, 10]. The potential of shock control bumps for normal shock control has been widely demonstrated despite their sensitivity to shock position and changes in flow conditions [11]. If the normal shock impinges away from its design position, additional shock and expansion structures develop, leading to worsened performance [12].

Aircraft and engine components are made of relatively flexible materials, which may deform under pressure loads. The interplay between surface deformations and the SBLI properties, an example of fluid–structure interaction, has become a subject of recent research interest in the context of adaptive shock control. Some groups have investigated dynamic shock control via vibrating surfaces [4, 13], while others have focused on static control with steady contoured

surfaces [6, 14, 15]. In this sense, steady flexible panels have been suggested as a simple form of passive oblique shock control, in a manner analogous to shock control bumps for transonic applications [6]. Previous studies on oblique SBLIs on flexible surfaces have highlighted potential reductions in the size of the separation region with increasing surface curvature [4, 6], a first step towards flow control.

For flexible panels to realize their potential as a practical means of oblique shock control in engine inlets, they must provide reduced total pressure losses. Some numerical investigations [5, 16] have suggested that contoured surfaces can lead to improved downstream stagnation pressure. No experimental confirmation of this currently exists, due to the technical challenges in measuring accurate stagnation pressure profiles in supersonic flows, particularly within the boundary layer. Nevertheless, the wall pressure distributions in Tan et al. [6] show that, for some shock positions, flexible panels can lead to more efficient flow compression upstream of the impinging oblique shock, potentially weakening the interaction and reducing losses.

Oblique SBLIs are also common in aircraft component–component interactions. For example, a supersonic aircraft with externally-mounted stores (such as fuel tanks or missiles) would experience an oblique shock impinging on the fuselage. In these cases, the incident shock is often followed by an expansion, which counters many of the effects of the SBLI by imposing a favourable pressure gradient. A simple way to produce an oblique shock in a wind tunnel is with a wedge-shaped plate, often referred to as a “shock generator". By necessity, these devices also introduce an expansion fan, as they must return the flow parallel to the freestream some distance downstream of the compression. Studies on oblique SBLIs often try to decouple these effects, either by increasing the SBLI–expansion distance [17] or by modifying the shock generator geometry [18]. The study of how this expansion affects flow properties is of interest, since component–component interactions in real aircraft usually produce similar shock–expansion structures. Studies on flat surfaces [17, 19] have found reductions in the separation length as the expansion is brought closer to the SBLI. Nevertheless, this interplay has not been explored on flexible surfaces thus far.

In this context, this study investigates the suitability of using steady flexible surfaces deforming under pressure loads for static oblique shock control. Experiments are conducted at Mach 2.0 in the Imperial College supersonic wind tunnel on a thin aluminium plate, using shock generators with 10° wedge angles. By varying the shock generator thickness, the effect of changing the distance between the shock and the expansion impingement points is studied. Particular focus is given to small SBLI–expansion distances, typical of those in aircraft component interactions. Similarly, the effects of changing the streamwise shock impingement point, at constant SBLI–expansion distance, are also explored. The experimental setup is described in Sec. II, while the results are presented and discussed in Sec. IV.

The experimental setup did not allow the reconstruction of the downstream total pressure profile. In order to overcome this, all experimental test cases have been replicated in two-dimensional Reynolds-averaged Navier Stokes (RANS) simulations in order to obtain downstream total pressure profiles. In these, the experimental wall profiles measured using photogrammetry are imposed as solid boundaries. Further details regarding the models and assumptions

in the numerical simulations are examined in Sec. III. Finally, the numerical results are validated and discussed in Sec. IV.E.

II. Experimental Methods

Experiments were performed in the Imperial College London (ICL) supersonic wind tunnel, a blow-down facility supplied with dry air from tanks pressurized to 2.7 MPa. The tanks provide sufficient compressed air for run-times of approximately 40 s, followed by a recharging time of several hours. Flow conditions at the settling chamber are controlled by a pneumatic valve that regulates stagnation pressure using a PID controller. For the present investigation, the tunnel was fitted with a Mach 2.0 supersonic nozzle. The flow conditions in the wind tunnel were characterized by Threadgill & Bruce [20], who reported an incoming boundary layer thickness $\delta = 5.87$ mm just upstream of the region of interest in this study.

The flexible plate was installed in the test section of the tunnel, which has a square cross-section and dimensions 727 mm long × 150 mm wide × 150 mm tall. A schematic diagram of the test section, along with the fitted equipment and the coordinate system, is shown in Fig. 1.

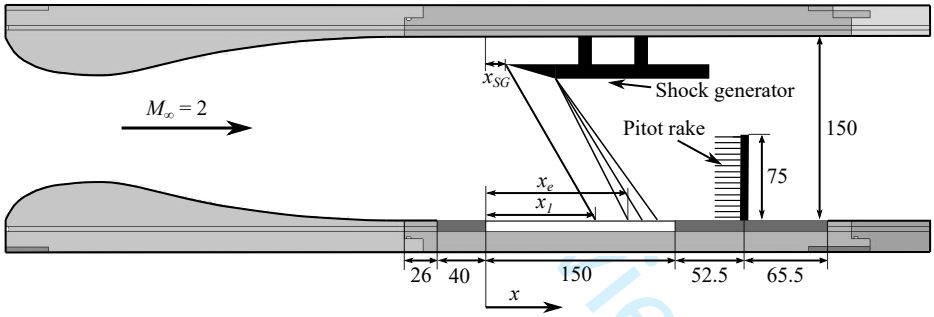

Fig. 1 Wind tunnel nozzle and test section, labeled with the relevant geometric parameters. Dimensions in mm.

Oblique shocks in the test section were produced using shock generators, which are wedge-shaped plates as shown in Fig. 1. As the flow turns around the convex corner on the underside of the shock generator, an expansion develops. All the shock generators in this study had a spanwise width of 148 mm and a wedge angle of $\theta = 10°$. The shock generators were attached to the top of the tunnel by two actuated mounts. The points x_1 and x_e in Fig. 1 respectively correspond to the inviscid shock and expansion impingement points on an undeformed flat plate.

The flexible plate assembly is made of the aluminum alloy Al 7075-T6 and has the same basic design as those described in Jinks et al. [21] and Tan et al. [6]. The plate was designed against flutter using the criterion in Dowell [22]. It contains a thin panel of length $a = 150$ mm, width 149 mm, and thickness $h = 0.6$ mm. The two longitudinal ends of the flexible plate are clamped to supports, while the two sides are free. A 0.5 mm gap exists between either side of the plate and the wind tunnel's walls. Each support was bolted to the wind tunnel floor at four points. Further details

regarding the plate design and mounting may be found in the Supplemental Materials. The flexible portion of the plate contains a total of 15 pressure tappings placed along the centerline, with the upstream support containing two additional tappings. Following the setup in Tan et al. [6], three aluminum spacers, each of thickness 0.4 mm, were slotted underneath the plate assembly to constrain end displacements.

Underneath the flexible panel, there sits a small chamber, known as the "cavity", sealed at all points except for the two sides of the plate and for the hole drilled for the Pitot rake tubes, which is itself partially blocked by these tubes. Since the mean flow is not isolated from the cavity, there is some leakage of air from the cavity into the flow. The difference between the pressures in the cavity (referred to as "cavity pressure", P_c) and in the flow is what drives plate deformations.

The plate assembly is fitted with a vertical Pitot rake positioned downstream of the flexible portion as shown in Fig. 1. The rake has a total of 15 Pitot probes for a total height of 75 mm, although only the 11 lowest ones were sampled. The probes are 5 mm apart, with the first one placed 3 mm above the surface. Since the bulk flow downstream of the plate is still supersonic, the pressure measured by these probes ("Pitot pressure", P_p), is not the same as the stagnation pressure. The Pitot rake did not contain static pressure tappings, and therefore, the experimental stagnation pressure could not be calculated. Due to this, numerical simulations were used to estimate the downstream total pressure, and their calculated Pitot pressures were compared to the experimental ones for verification. Pressure measurements were taken using a Netscanner pressure transducer, sampling at 100 Hz. Pressure data was sampled for a period of 5 s for each test case once the settling chamber pressure had reached the steady-state. Moreover, the standard deviation was recorded for each measurement, and this was used as a measure of experimental errors.

Schlieren photography was employed to observe the flow structure above the flexible panel. A Z-type configuration was used, in which light from a Thorlabs MCWHL5 LED point source with a Thorlabs LEDD1B driver was reflected on two 200 mm diameter concave mirrors with a focal length of 1200 mm. The light was focused on an aperture with a vertical knife-edge, blocking the right-half of the light. Schlieren images were recorded with a Phantom v641 high-speed camera.

Point-tracking photogrammetry was used to reconstruct the 3D bump profile. Following the work of Gramola et al. [23], eighty 12-bit coded targets, each of thickness 20 µm, were attached to the surface of the plate. The motion of these targets was recorded using four synchronized Phantom Miro 310 cameras, placed at different angles around the viewing panels of the working section. All the cameras had a resolution of 1280×800 pixels and recorded at the same frequency as the pressure transducers (100 Hz). Further details regarding the setup, calibration and post-processing may be found in Gramola et al. [23]. For every run, a photograph was extracted from each of the four cameras once the plate deformations were steady. These images were subsequently processed using the commercial software *PhotoModeler Motion* [24], allowing the reconstruction of the 3D bump profile.

The separation region was observed using surface oil flow visualisation. For these experiments, the photogrammetry

targets were removed. An oil mixture was injected onto the surface of the tunnel floor through two holes in the plate assembly, which are 60 mm apart and 8 mm downstream of the front of the panel. The oil was a mixture of oleic acid, titanium dioxide and kerosene, in the following proportions: for every 17 g of kerosene, 10 g of titanium dioxide and 11 drops of oleic acid. Oil motion was filmed through the sidewall viewing panels using one of the photogrammetry cameras. Since oil flow images were taken at an angle, a dewarping process was necessary to correct for the effects of perspective and plate deformations. For this purpose, the geometric method in Stamatopoulos et al. [25] was implemented, consisting in mapping pixels on a curved surface to a 2D rectangular area. Once the dewarped images were obtained, these were used to produce streakline schematic diagrams.

A parametric study was performed by testing several shock and expansion impingement points. A parameter affecting the SBLI–expansion distance is the tunnel aspect ratio $\mathcal{AR}$, which is defined here as the effective width-to-height ratio of the wind tunnel test section, with the height being measured from the wind tunnel floor to the tip of the shock generator. Alternative definitions exist; for example, some authors [26, 27] define an unrelated "viscous aspect ratio". A high aspect ratio, with a shock generator close to the floor, would provide larger SBLI–expansion distances; however, it would also interfere with the photogrammetry equipment, covering the targets, and could cause tunnel unstart. In order to prevent this, experiments were conducted at a constant aspect ratio of $\mathcal{AR} = 1.25$. This choice provides an adequate maximum SBLI–expansion distance (17 mm) whilst ensuring that the photogrammetry targets are not covered. Because of this choice, the SBLI–expansion distance was varied using shock generators of different thicknesses.

A total of 21 test cases were examined using three different shock generators thicknesses ($t_{SG} = 11.3$ mm, 9.5 mm and 8.0 mm) with a constant wedge angle $\theta = 10°$. The shock generator streamwise location was varied between tests to obtain seven streamwise shock positions, in the range $0.27 \leq x_1/a \leq 1.01$, for each shock generator thickness. The different shock generator thicknesses provide three different SBLI–expansion distances $x_e - x_1$ (following the notation in Fig. 1) to be tested: 17, 8 and 1 mm. It should be noted that, in calculating these distances, it was assumed that the expansion crosses the reflected shock unhindered as suggested by Grossman & Bruce [17]. Similarly, the effects of plate deformations, which are not known in advance, on x_1 and x_e were also ignored. All test cases were conducted with a settling chamber pressure ratio $P_{0,s}/P_a = 1.80$, which was expected to provide fully supersonic flow in the test section.

Moreover, six additional test cases were conducted with the oil flow visualisation setup. These explore the impact of shock streamwise position and shock generator thickness on flow separation.

III. Numerical Simulations

A numerical investigation was conducted using the commercial Computational Fluid Dynamics (CFD) software *Star-CCM+* [28] in order to quantify the effects of the flexible plate on downstream total pressure recovery. Fully-turbulent, steady simulations were performed in a two-dimensional domain to reduce the computational costs. In these, the RANS equations were solved via the finite volume method using a coupled flow model, which solves the mass and

momentum equations simultaneously. Air was assumed to behave as a calorically perfect gas, with a viscosity governed by Sutherland's law.

A turbulence model was used to close the RANS equations. Popular choices for numerical simulations of flows with shock–boundary layer interactions include the one-equation Spalart-Allmaras model [15, 29], and the two-equation Menter's shear-stress transport (SST) k-ω model [3–5]. Among these, the Menter SST k-ω model was selected due to its superior performance in flows with strong adverse pressure gradients and separation [4, 30].

The main boundary conditions in the simulations are the inlet conditions (pressure and temperature) and velocity profile, and the outlet pressure. The inlet velocity profile was calculated with a one-seventh power law, given by Eq. (20.6) in Schlichting [31], using the boundary layer parameters measured by Threadgill & Bruce [20] for the ICL supersonic wind tunnel. This provides an incompressible shape factor $H = 1.286$, which matches the value reported by Threadgill & Bruce [20], $H = 1.28$. Both the inlet and outlet static pressures are set constant and equal to $P_\infty = 23.3\,\text{kPa}$, which is the static pressure corresponding to an $M_\infty = 2$ flow with $P_0 = 1.8\,\text{atm}$.

The computational domain is shown in Fig. 2. All walls are assumed to be adiabatic, and the bump profiles for each simulation are obtained from photogrammetry measurements.

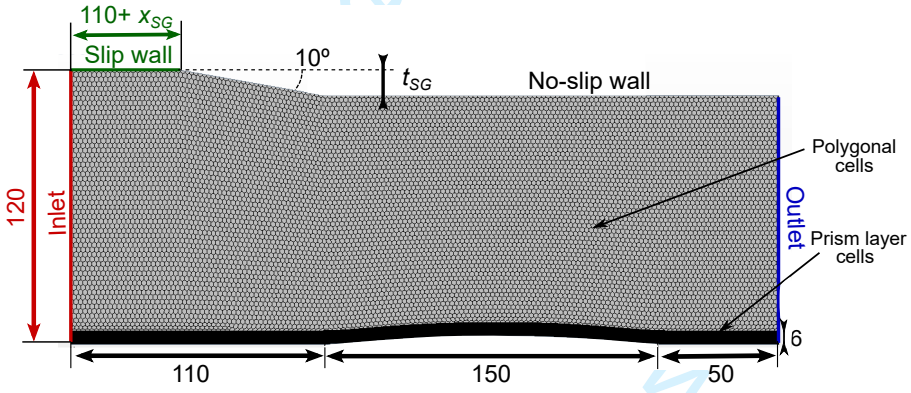

Fig. 2 Computational domain, labeled with dimensions and boundary conditions. Dimensions in mm.

Due to the curvature of the flexible plate, a polygonal mesher was selected. In addition, a prism layer mesh, with quadrilateral cells of high aspect ratio, was used along the bottom boundary to better capture the boundary layer profile. The near-wall cell thickness was selected so that $y^+ \approx 1$. To ensure an adequate resolution of the boundary layer, a total of 150 prism cells were used in the wall-normal direction for a total prism layer thickness of 6 mm, which is slightly larger than the initial boundary layer height, $\delta = 5.8\,\text{mm}$.

A mesh refinement study was conducted in order to determine the target surface size of the polygonal cells l, which is the reference edge length that the mesher aims to achieve. The study was conducted on a computational domain similar to the one in Fig. 2, but with a flat bottom boundary. Fig. 3 shows the skin-friction coefficient distributions predicted by each of the different meshes. Some differences in the skin friction distributions can be seen as the mesh is

refined from $l = 2$ mm to $l = 0.3$ mm; whereas further refining with cell sizes smaller than $l = 0.3$ mm only result in marginal changes, indicating convergence. Based on the plots in Fig. 3, the $l = 0.2$ mm mesh has been selected, as this provides an adequate prediction of the converged skin-friction distribution at a lower cost than the most refined mesh. This choice of cell size results in meshes of the order of 1 million cells; however, the exact number of cells varies as the shock generator position is changed. A sample mesh is shown in Fig. 2, where a coarser mesh is presented for clarity.

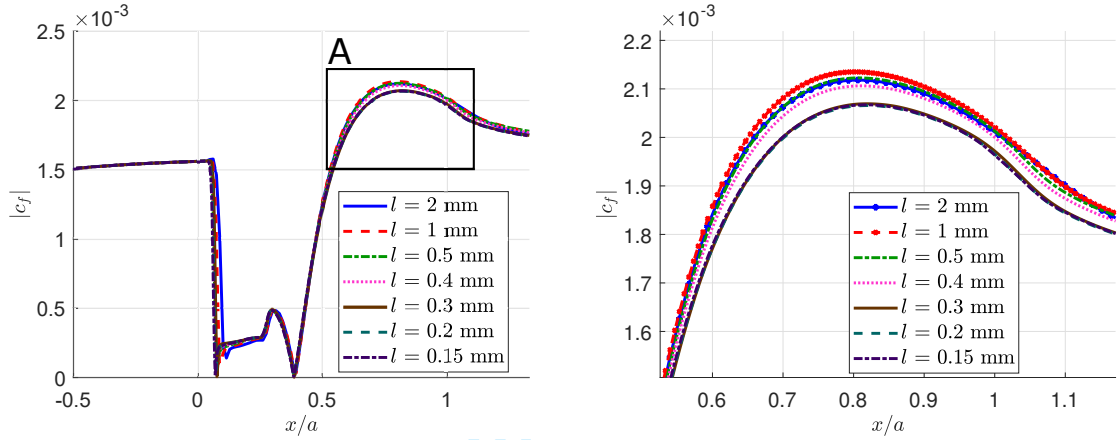

(a) Skin-friction distribution **(b) Detailed view of region A**

Fig. 3 Skin-friction coefficient distributions for different cell sizes.

In order to quantify the effects of the flexible plate on downstream stagnation pressure, all the experimental test cases were simulated. To provide baseline results, three additional simulations were conducted on a flat surface, one for each shock generator thickness.

IV. Results

All streamwise distances in this study are measured with respect to the front (leading edge) of the flexible panel, where $x = 0$ as defined in Fig. 1. Similarly, the experimental test cases are identified according to their shock generator thickness t_{SG} and their inviscid shock impingement point normalized by the plate length, x_1/a. Cavity pressure was approximately constant during a run and was found to vary in the range $0.27 \leq P_c/P_{0,s} \leq 0.35$ across different test cases. The cavity pressure measured during each test is shown in the Supplemental materials.

A. Flow morphology

The flow morphology of an SBLI on a flexible panel is different from that on a flat surface, with plate curvature introducing additional shocks and expansions. A typical schlieren image, obtained with the flexible assembly, is shown in Fig. 4, and has been labeled with shock and flow structures that are common to all test cases.

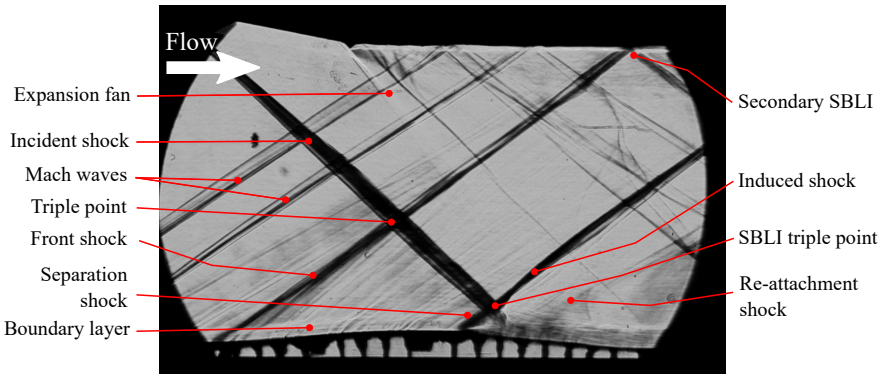

Fig. 4 Schlieren image corresponding to the t_{SG} = 11.3 mm, x_1/a = 0.87 test case, labeled with the main flow structures

The presence of the deflected flexible panel results in the formation of a shock at the front of the bump, labeled as the "front shock" in Fig. 4. This shock imposes an adverse pressure gradient but is not strong enough to cause boundary layer separation. The front shock intersects the incident shock at a downstream position, giving rise to an additional triple point, which is the intersection point itself. Moreover, a secondary, weaker SBLI can also be seen at the point where the front shock is incident on the shock generator. The expansion that forms around the convex corner on the lower side of the shock generator has also been labeled in Fig. 4, although this is barely visible due to the chosen knife-edge configuration.

The thickness of a shock wave should be of the same order as the molecule's mean free path [32]. The apparent thickness of the shocks in Fig. 4 is attributed to variations in flow conditions across the span of the tunnel, including the sidewall boundary layers.

1. Effect of changing shock impingement point

As the shock generator is moved downstream, some changes in the flow structures can be observed. These are illustrated in Fig. 5, which shows a comparison of schlieren images taken with different streamwise shock positions.

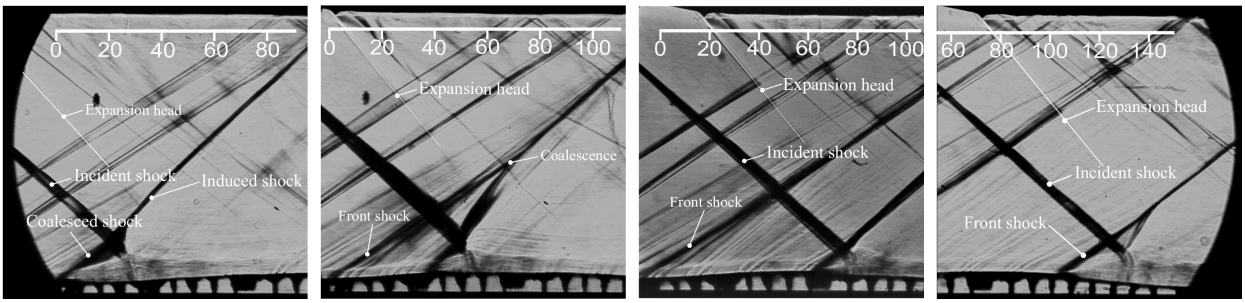

(a) x_1/a = 0.34 **(b) x_1/a = 0.57** **(c) x_1/a = 0.72** **(d) x_1/a = 1.01**

Fig. 5 Schlieren images obtained at four shock generator streamwise positions, with a constant t_{SG} = 11.3 mm shock generator. Only a portion of the images is shown. Scales in mm.

When the shock impinges near the leading edge of the flexible panel, a large separation bubble with a high upstream influence develops, as shown in Fig. 5(a). The front shock associated with concave curvature at the front of the panel and the SBLI separation shock coalesce into a single, strong shock. As the shock generator is moved downstream, the front and separation shocks split, and an independent (smaller) SBLI becomes visible; however, the front shock and the SBLI's induced shock still coalesce further downstream, as shown in 5(b). This phenomenon had been previously observed by Tan et al. [6], who referred to the resulting structure as a "tilted λ-shock". When the shock impingement point is moved further downstream, this shock coalescence is no longer observed, as seen in 5(c) and 5(d). If the shock impinges far downstream, as in 5(d), a large SBLI with a high upstream influence is observed.

2. Effect of changing shock generator thickness

The distance between the shock and the shock generator's expansion fan depends on the shock generator thickness, with thinner shock generators leading to smaller SBLI–expansion distances. The effect of varying the shock generator thickness on the flow structures, whilst maintaining the same shock generator streamwise position, is shown in Fig. 6.

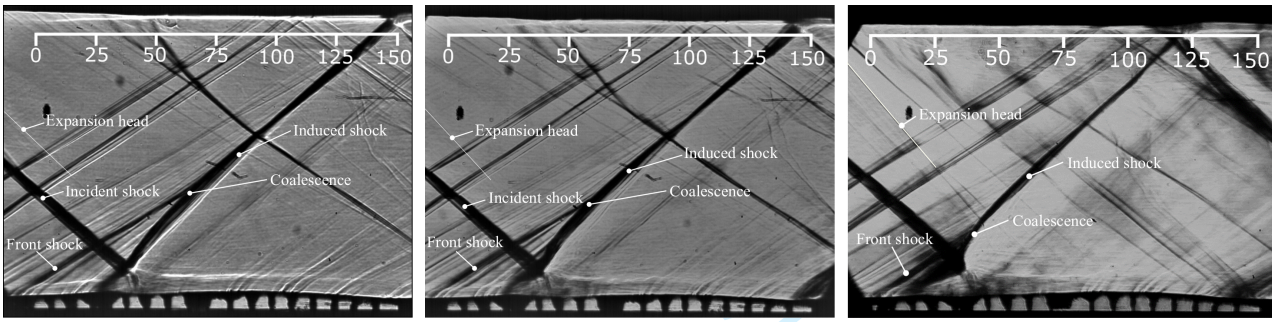

(a) t_{SG} = 8.0 mm **(b) t_{SG} = 9.5 mm** **(c) t_{SG} = 11.3 mm**

Fig. 6 Schlieren images obtained with shock generators of different thicknesses at the same streamwise position x_1/a = 0.42

Figure 6 shows that, as the expansion fan is moved further away from the SBLI, the size of the SBLI increases. This is consistent with the results of previous experiments on a flat surface by Grossman & Bruce [17]. The vertical position of the SBLI's triple point is also found to increase with increasing SBLI–expansion distance. These changes in SBLI structure are related to changes in shock-induced separation, as will be explored in Sec. IV.D.

3. Interaction lengths

In addition to providing means to visualise flow structures, the schlieren images can also be used to estimate the interaction length L_{int}, which is the upstream distance across which the shock pressure rise is smeared. In this study, the interaction length has been measured as shown in Fig. 7(a). The pixel measurement method introduces uncertainty in the interaction length measurements. This has been estimated from the schlieren images to be approximately ±1 mm.

Additional errors are caused by non-negligible shock thicknesses and optical distortion within the boundary layer; however, these have not been quantified.

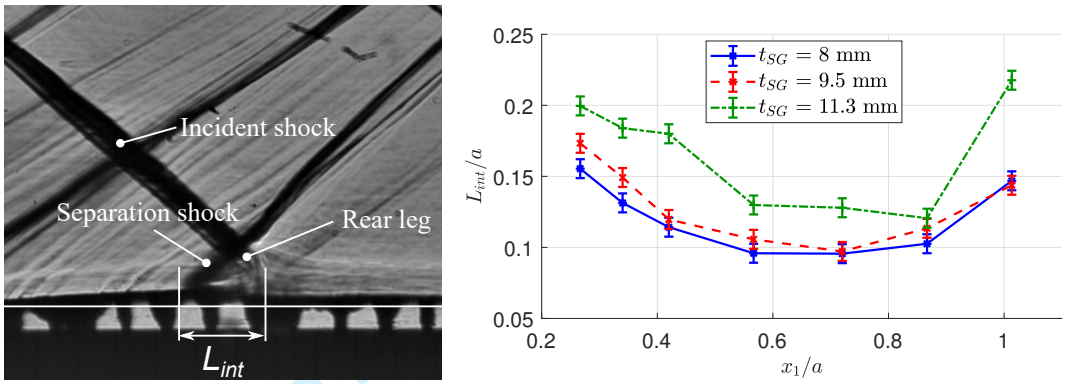

(a) Definition **(b) Interaction length plot**

Fig. 7 (a) Interaction length definition, and (b) measured interaction lengths against normalised inviscid shock impingement point.

The measured interaction lengths are plotted against the inviscid shock impingement point in Fig. 7(b). The same trend is observed for all shock generator thicknesses: as the shock impingement point moves downstream, the interaction length decreases until it reaches a minimum when the shock impinges on the downstream half of the plate, before increasing again when the shock impinges near the trailing edge. Since the interaction length is related to the size of the separation bubble, the results in Fig. 7(b) suggest that smaller separation regions could be obtained if the shock impinges on the middle region of the bump. Moreover, a reduction in the upstream influence is consistently observed when the shock generator thickness is decreased.

B. Static pressure distributions

Static pressure distributions were measured using 17 static pressure tappings placed along the centerline of the flexible plate and of the upstream mounting block. Pressure data has been time-averaged over a period of 5 s.

1. Effect of shock impingement point

The static pressure distributions obtained with the $t_{SG} = 9.5$ mm shock generator are shown in Fig. 8 and have been normalized by the settling chamber stagnation pressure $P_{0,s}$. The pressure distributions obtained with the remaining shock generators share the main trends in Fig. 8.

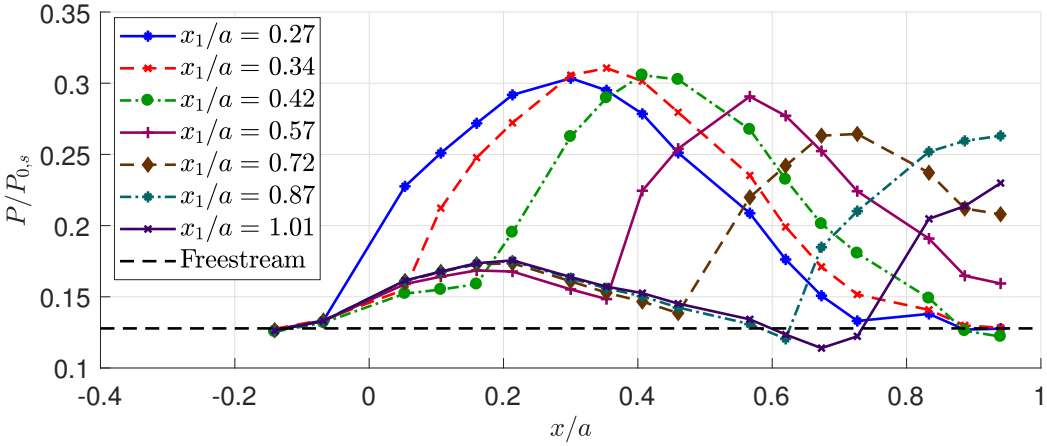

Fig. 8 Normalized static pressure distributions along the plate's centerline at varying shock impingement points, corresponding to the t_{SG} = 9.5 mm test cases.

Upstream of the flexible plate, all pressure distributions lie close to the isentropic pressure ratio at $M_\infty = 2$, which is shown as a black dashed line in Fig. 8.

A critical factor affecting the pressure distributions is surface curvature, d^2w/dx^2, which in a supersonic flow is related to the pressure gradient. In the downstream direction, pressure initially varies due to plate bending, followed by a large pressure rise as a result of the impinging shock. The initial pressure rise due to plate bending can be seen to varying extents in all shock streamwise positions x_1, but it is more noticeable when the shock impinges near the trailing edge of the plate. The point of maximum pressure solely due to plate deformation does not correspond to the bump's peak; instead, maximum static pressure (ignoring the shock) is reached when plate curvature as seen by the flow changes sign from concave to convex.

The SBLI pressure rise occurs upstream of the ideal inviscid shock impingement point, as a result of the shock smearing due to the interaction. After the initial sharp SBLI pressure rise, pressure continues to increase until it reaches a maximum and then decreases. This decrease in static pressure (a favourable pressure gradient) occurs because of two factors: the shock generator expansion and the negative plate curvature. The flow would be expected to re-attach in this region of favourable pressure gradient; hence, the distance between the pressure rise due to the shock and the pressure peak may be taken as a crude indicator of the separation length.

Previous investigations on the effect of the shock streamwise positions by Tan et al. [6] hypothesized the existence of a streamwise shock impingement point that would result in maximum static pressure on the plate. Furthermore, they also suggested that this would translate into improved downstream total pressure recovery due to shock weakening upstream of the SBLI. As seen in Fig. 8, this maximum static pressure indeed exists. For the t_{SG} = 9.5 mm shock generator, it corresponds to the $x_1/a = 0.34$ case, although this changes in the range $0.34 \leq x_1/a \leq 0.57$ when other shock generators are used. This maximum in the static pressure distributions occurs when the shock impinges on the

bump near the point of zero plate curvature, i.e. where there is a peak in pressure rise due to the bump shape alone. As a result, the flow undergoes a continuous compression due firstly to the bump, and subsequently the SBLI. When the shock is further downstream, re-expansion due to negative plate curvature reduces the maximum post-shock static pressure.

2. Effect of SBLI–expansion distance

When the expansion is moved closer to the SBLI, some changes in the static pressure distributions are anticipated since the expansion imposes a favourable pressure gradient. The effect of changing the shock generator thickness on the static pressures is shown in Fig. 9. Four subfigures are included, corresponding to different shock streamwise positions.

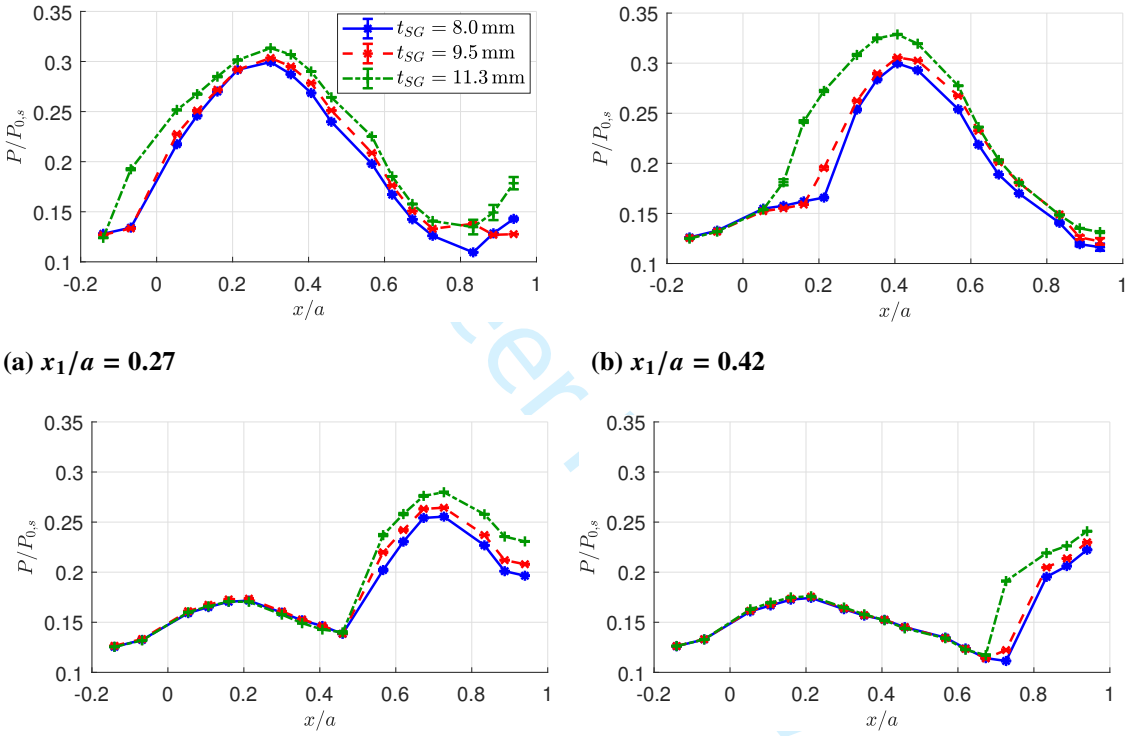

(a) $x_1/a = 0.27$ **(b) $x_1/a = 0.42$**

(c) $x_1/a = 0.72$ **(d) $x_1/a = 1.01$**

Fig. 9 Normalized static pressure distributions along the plate's centerline for changing shock generator thicknesses at four shock impingement points. Error bars represent one standard deviation.

Firstly, an increase in the SBLI strength is seen as the expansion is moved away from the shock, as shown by the greater post-shock static pressures. In addition, the SBLI pressure rise occurs further upstream as t_{SG} increases, implying greater interaction lengths. A similar trend had been previously observed by Grossman & Bruce [17] on flat surfaces. Overall, these increases in pressure and upstream influence with shock generator thickness are in line with the observations in Fig. 6, where larger interaction lengths were seen in the schlieren images with increasing SBLI–expansion distance. Upstream of the SBLI pressure rise, the pressure distributions are almost identical for all three shock generator thicknesses, suggesting that these pressure differences only result in marginally different plate

profiles.

C. Plate deformations

Using photogrammetry, the three-dimensional plate deformations have been extracted at the locations of the photogrammetry targets. Plate deformations were found to be steady once the starting shock was swallowed, and no vibrations were recorded. A sample 3D plate profile is shown in Fig. 10, where the detected positions of the coded targets are indicated with blue markers.

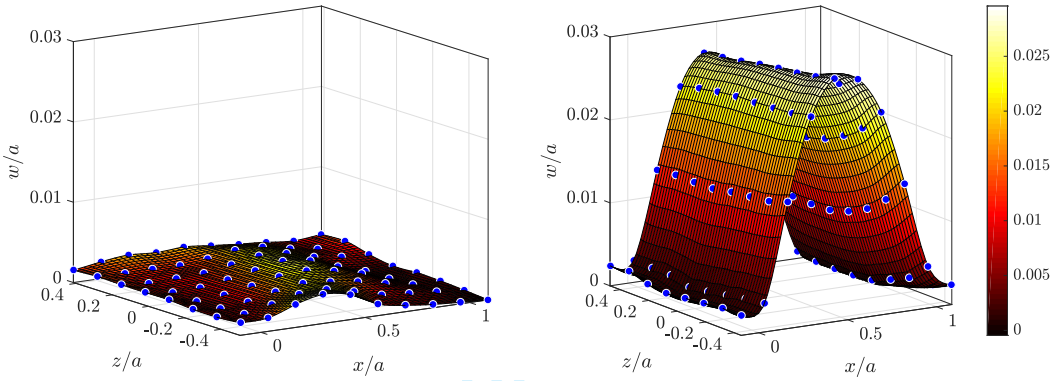

(a) Wind-off **(b) Wind-on**

Fig. 10 Sample three-dimensional plate profiles, corresponding to the $t_{SG} = 11.3$ mm, $x_1/a = 0.72$ test case. Deformations are interpolated with thin-plate smoothing splines.

Some three-dimensionality in the initial bump profile can be seen in Fig. 10(a); however, the maximum deformations are of the order of 0.5 mm, and are small compared to the wind-on deflections. These static deformations are caused by small stresses introduced by the mounting procedure. The wind-on profile in Fig. 10(b) is approximately two-dimensional, showing only small spanwise variations. Because of this, only the spanwise-averaged deformations will be considered in subsequent sections. Nevertheless, the profile in Fig. 10(b) does exhibit some degree of three-dimensionality, with slightly higher deflections near the two free ends of the plate.

The changes in static pressure due to different shock impingement points affect plate deformations. The spanwise-averaged plate profiles corresponding to the $t_{SG} = 8.0$ mm and $t_{SG} = 9.5$ mm test cases are shown in Fig. 11.

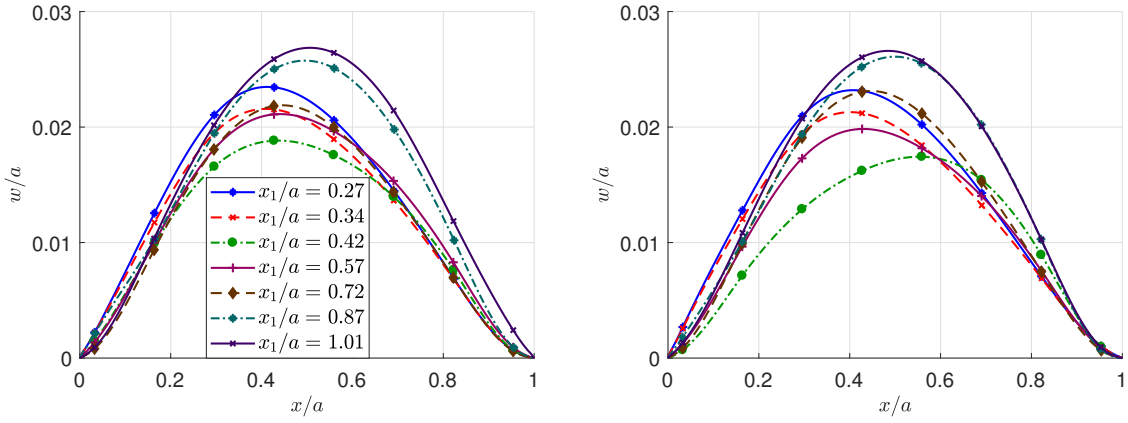

(a) t_{SG} = 8.0 mm **(b) t_{SG} = 9.5 mm**

Fig. 11 Spanwise-averaged plate deformations for varying shock impingement position, interpolated with thin-plate interpolation splines. Markers indicate the streamwise locations of the photogrammetry targets.

Plate profiles are found to change significantly with shock position. Fig. 11 shows that there is a minimum in maximum plate deflection for $x_1/a = 0.42$, while this increases for shock locations upstream and downstream of this position.

D. Oil flow visualisation

Surface oil flow visualisation has been used to observe the topology of the separation region by injecting oil into the boundary layer at two spanwise stations. Some representative oil flow frames are shown in Fig. 12 for different streamwise shock impingement positions. In order to aid visualisation, the contrast in these images has been modified via histogram equalisation and streaklines have been added. All figures have been marked with the streamwise and spanwise extents of the separation regions.

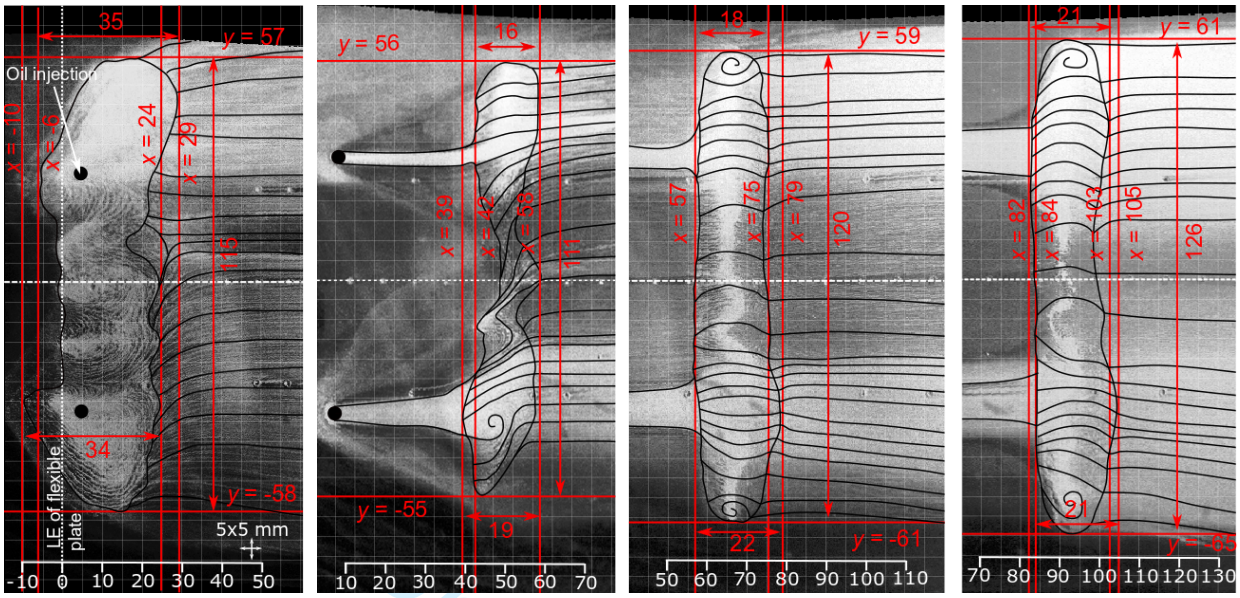

(a) $x_1/a = 0.27$ **(b)** $x_1/a = 0.42$ **(c)** $x_1/a = 0.57$ **(d)** $x_1/a = 0.72$

Fig. 12 Oil flow visualisation images for varying shock impingement point, with a constant $t_{SG} = 8.0$ mm. Streakline schematics are superimposed.

All the images in Fig. 12 display a similar trend: most of the oil is concentrated in two distinct separation cells, connected via a thinner region of cross-flow. This is, however, expected as the oil is injected at two spanwise locations. When the shock impinges near the front of the bump, such as in Fig. 12(a), a large separation bubble is formed.The flowfield in Fig. 12(a) should be interpreted with some caution relative to the other test cases since the oil was injected directly into the separation bubble and the impact of this on the separation region is unknown.

The separation bubble in Fig. 12(a) is large, with a length $L_{sep} = 35 \pm 4$ mm in the streamwise direction and a width of 115 mm. As the shock impingement is changed from $x_1/a = 0.27$ to 0.42 in Fig. 12(b), the length of the separation region is approximately halved, with the bubble having $L_{sep} = 18 \pm 3$ mm and a width of 111 mm. When the shock moves further downstream, both the length and width of the separation bubble increase slightly. This suggests the existence of a streamwise shock position that results in a separation bubble of minimum size.

Figure 13 shows the effects of changing the shock generator thickness on the topology of the separation region. As the expansion is moved away from the SBLI, the separation length increases. This growth of the separation region occurs via an increase in the SBLI's upstream influence, as the re-attachment point remains approximately the same in all three cases. Both the increase in size of the separation bubble and the invariance in the re-attachment point with increasing SBLI–expansion distances are consistent with the observations of Grossman & Bruce [17] for SBLIs on flat surfaces.

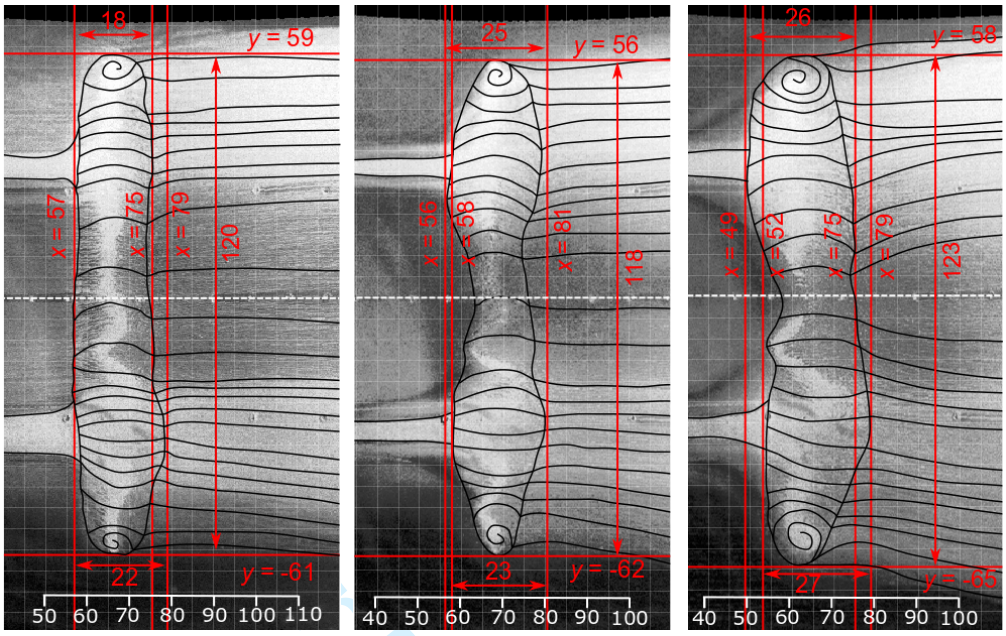

(a) t_{SG} **= 8.0 mm** **(b)** t_{SG} **= 9.5 mm** **(c)** t_{SG} **= 11.3 mm**

Fig. 13 Oil flow visualisation images for different SBLI–expansion distances, at a constant $x_1/a = 0.57$

The separation and re-attachment streamwise locations, x_s and x_r respectively, are tabulated in Table 1 as measured from the oil flow images. These were measured along the streamlines emanating from the oil injection ports, where oil density is greatest. The separation length (defined as $L_{sep} = x_r - x_s$) and the ratio of the interaction length (as shown in Fig. 7) to the separation length are also included.

Table 1 List of separation and re-attachment points, as measured in the oil flow images.

t_{SG} (mm)	x_1/a	x_s (mm)	x_r (mm)	L_{sep} (mm)	L_{int}/L_{sep}
8.0	0.27	−8 ± 2	26 ± 2	34 ± 4	0.70 ± 0.08
	0.42	40 ± 2	58 ± 1	18 ± 3	1.0 ± 0.2
	0.57	57 ± 1	77 ± 2	20 ± 3	0.7 ± 0.1
	0.72	83 ± 1	104 ± 1	21 ± 2	0.69 ± 0.06
9.5	0.57	57 ± 1	81 ± 1	24 ± 2	0.67 ± 0.06
11.3	0.57	50 ± 2	77 ± 2	27 ± 4	0.7 ± 0.1

E. Numerical simulations

In order to explore the effects of the flexible plate on the downstream total pressure recovery, all the experimental test cases have been reproduced in two-dimensional steady simulations. In these, the experimental spanwise-averaged plate profiles were imposed as solid boundaries. The simplified 2D simulations do not capture some important SBLI effects, such as flow unsteadiness, flow bleeding/injection due to the cavity, and the effect of the sidewall boundary layers. Due to these simplifications, some differences between the experimental and simulated flowfields are anticipated. The experimental and numerical results are compared in Sections IV.E.1-3. The calculated stagnation pressure profiles, for which no experimental validation was available, are presented in Section IV.E.4.

1. Flow structures

In order to visualise the computational flowfield, the spatial distribution of some scalar quantity may be considered. Fig. 14 compares a representative Mach number field obtained with the numerical simulations to its corresponding experimental schlieren image.

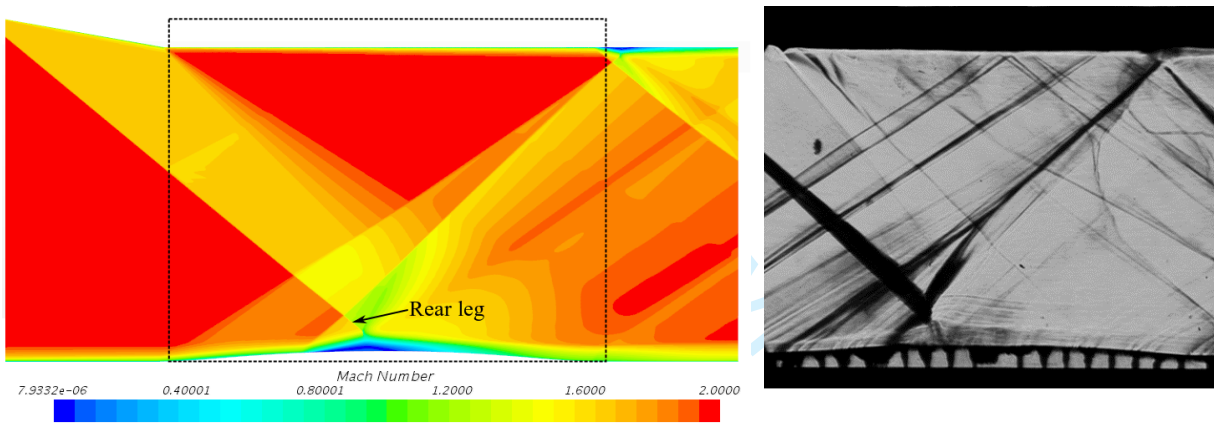

(a) Mach number, CFD **(b) Schlieren, experimental**

Fig. 14 Comparison of the Mach number field obtained with CFD and an experimental schlieren image, both corresponding to the t_{SG} = 11.3 mm, x_1/a = 0.57 test case. The schlieren image in (b) corresponds to the region inside the dashed rectangle in (a).

Figures 14(a) and (b) both show similar flow structures. As shown in 14(a), the numerical simulation predicts the coalescence of the front and induced shocks observed in experiments; however, these shocks intersect further downstream than in 14(b). This is in part due to differences in the induced shock angle, which is visibly shallower in 14(a) than in 14(b). Examining the SBLI itself, the numerical simulations predict a region of supersonic flow outside the separation bubble, as well as a clear SBLI rear leg. In contrast, the schlieren image shows that the flow downstream of the separation shock is highly unsteady, with a barely visible rear leg.

2. Static and Pitot pressure validation

Figure 15 compares the numerical static pressure distributions along the wind tunnel's surface to the experimental ones. In simulations, static pressures in the range $-0.73 \leq x/a \leq 1.33$ are available, but only a part of these are shown in order to ease comparison with the experiments.

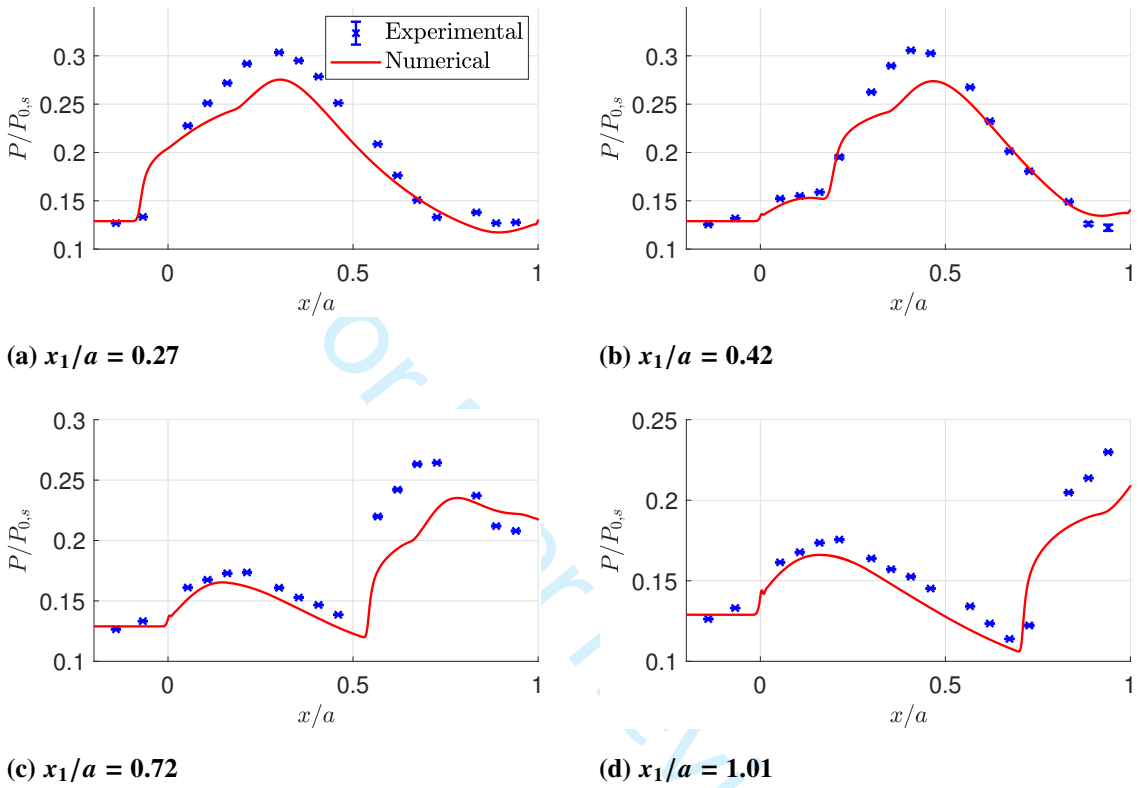

(a) $x_1/a = 0.27$ **(b) $x_1/a = 0.42$**

(c) $x_1/a = 0.72$ **(d) $x_1/a = 1.01$**

Fig. 15 Comparison of the normalized static pressure distributions, obtained with the $t_{SG} = 9.5$ mm shock generator. Error bars represent one standard deviation.

Upstream of the shock, the experimental and CFD pressure profiles agree well. The pressure rises due to plate curvature in Figs. 15(b-d) are very similar in experiments and CFD, with the pressure peak being approximately at the same streamwise location. Nevertheless, the numerical simulations slightly underestimate the pressure magnitude, potentially due to slightly inaccurate interpolated plate curvature, or the inability of the CFD simulations to accurately capture the boundary layer development.

A greater discrepancy between experiments and CFD can be seen after the shock impingement, with numerical simulations consistently underpredicting the magnitude (and hence the strength) of the SBLI pressure rise. These discrepancies between the experimental and RANS pressure distributions in the SBLI region had been observed in previous studies. As noted by Benek [33], the computed SBLI pressure rises in RANS simulations relax towards zero pressure gradient faster than in experiments.

All CFD simulations predict a two-step pressure rise due to the SBLI. This has also been observed in other numerical and experimental studies [4, 17]. Nevertheless, this two-step rise is not seen in the experimental pressure distributions. This can be partially attributed to the low spatial resolution of the experimental pressure measurements, which does not allow the complete reconstruction of the SBLI pressure rise. A better agreement between the CFD simulations and the experiments can be seen in the region downstream of the pressure peak (with a favourable pressure gradient) in Figs. 15(a) and (b).

A sensitivity study was conducted to explore the effects of changing the inlet boundary layer thickness (in the range $4 \leq \delta \leq 8$ mm) on the pressure distributions. A slight increase on the upstream influence, and a reduction in the pressure rise, were observed as the boundary layer thickness was increased. However, these changes are small compared to the discrepancies with experiments seen in Fig. 15.

The Rayleigh-Pitot equation, given by Eq. (8.80) in Anderson [32], has been used to calculate the numerical Pitot pressure at a station $x = 180$ mm, which is the location of the Pitot rake in experiments. Figure 16 compares the experimental and numerical Pitot pressures at four different shock impingement locations.

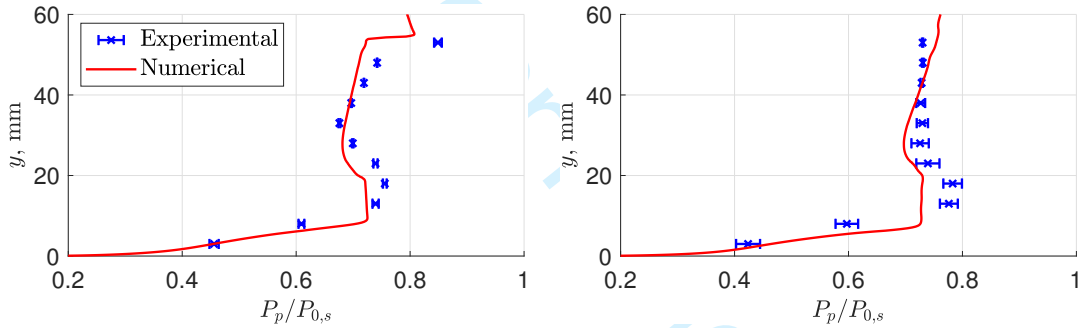

(a) $x_1/a = 0.27$

(b) $x_1/a = 0.42$

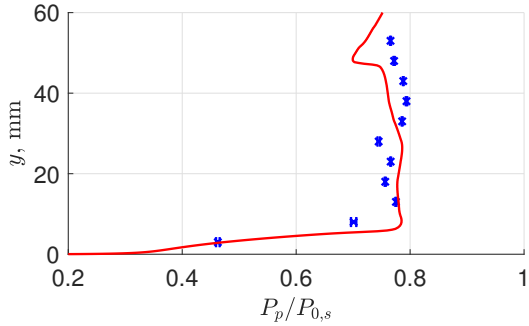

(c) $x_1/a = 0.72$

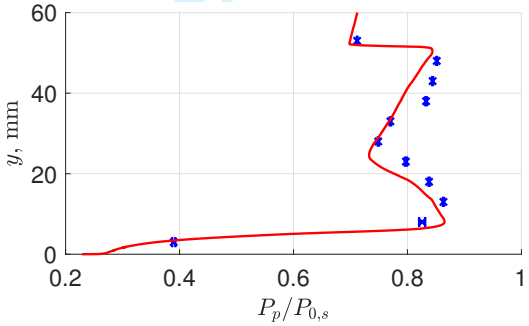

(d) $x_1/a = 1.01$

Fig. 16 Comparison of the normalized Pitot pressures recorded at $x = 180$ mm from experiments and numerical simulations, obtained with the $t_{SG} = 9.5$ mm shock generator. Error bars represent one standard deviation.

In general, the experimental and numerical Pitot pressure distributions show a good agreement. For example, the

numerical simulation in Fig. 16(d) correctly predicts the experimental Pitot pressure profile including the effects of the induced shock, which is responsible for the sudden decrease in the uppermost experimental Pitot measurement. However, CFD slightly underestimates the magnitude of the Pitot pressures in 16(d). The agreement between CFD and experiments is worse in 16(b) and (c). In 16(b), the experimental data displays some unsteadiness, shown by the large error bars, and this is not captured by the steady simulations.

Observing the boundary layer profile, for which only the data points at $y = 3$ mm and $y = 8$ mm are available in experiments, it can be seen that CFD simulations accurately capture the first experimental data point in all four cases, but consistently overpredict the Pitot pressure of the second one, at $y = 8$ mm.

3. Separation

A key factor in characterising an SBLI is the separation length. In simulations, the separation (x_s) and re-attachment points (x_r) were inferred from the region where $c_f < 0$. A sample skin-friction plot was shown in Fig. 3. Once these points were known, the separation length was calculated and the results are shown in Fig. 17. Moreover, a set of baseline (reference) values, calculated on a flat surface with different shock generator thicknesses and a shock impinging at $x_1/a = 0.57$, have been added as horizontal lines.

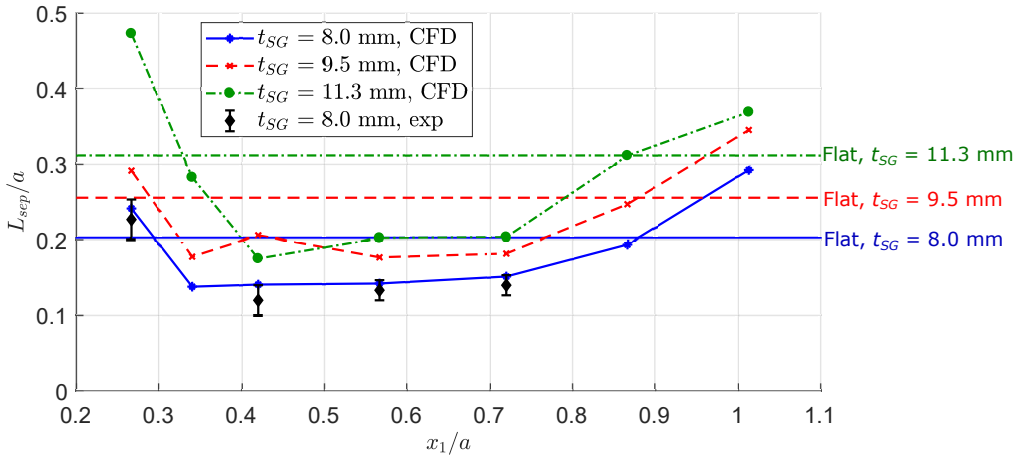

Fig. 17 Variation in separation length with shock impingement position.

Figure 17 shows that, if the shock impinges on the middle region of the bump ($0.34 \leq x_1/a \leq 0.87$), reductions of the order of 40 % in the separation length can be achieved with respect to the flat surface case. This is true for all shock generator thicknesses considered. To validate these predictions, the experimental results obtained with oil flow visualisation are shown superimposed, and these agree well with the CFD values. If the shock impinges too far upstream or downstream, performance degrades and separation lengths up to 45 % larger than in the flat surface case are observed.

Grossman & Bruce [17] reported that increasing the shock generator thickness resulted in increased separation lengths on a flat surface. As shown in Fig. 17, this is also true when the shock impinges on a deflected surface.

Furthermore, even though the flat surface separation lengths have been plotted as horizontal lines (independent of the shock impingement position), in reality, the separation length would be expected to increase slightly as the shock impinges further downstream due to boundary layer thickening.

4. Stagnation pressure

Figure 18 shows the downstream stagnation pressure profiles obtained with the $t_{SG} = 9.5$ mm shock generator, as predicted by simulations. All stagnation pressures have been calculated at $x = 180$ mm, as this was the location of the Pitot rake in the experiments.

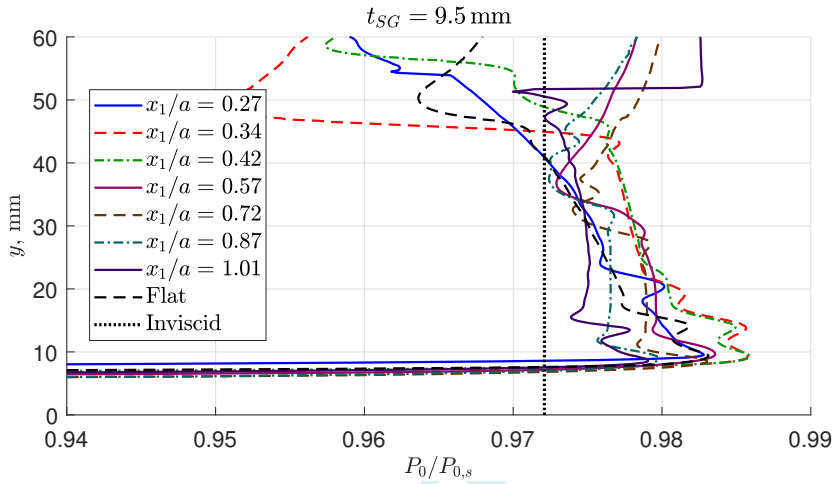

Fig. 18 Stagnation pressure profiles at $x = 180$ mm for varying shock impingement locations. Only values outside the boundary layer are shown.

Considering first the flow outside the boundary layer ($y > 10$ mm), it can be seen that the $x_1/a = 0.34$ and $x_1/a = 0.42$ shock positions provide the greatest stagnation pressure recovery, at least in the $10 \leq y \leq 45$ mm region. These are the shock impingement locations that also resulted in the highest peak static pressures in Fig. 8. Nevertheless, these two test cases show a sudden decrease in stagnation pressure for $y > 45$ mm, and this is caused by the coalescence between the front and induced shocks, as seen in Fig. 5(b).

In order to quantify the effects of the flexible plate on total pressure recovery, a recovery coefficient c_{rec} has been considered. This represents a mass-weighted average of the downstream total pressure, and is defined as

$$c_{rec} = \frac{\int_0^{y_{end}} \rho u \frac{P_0}{P_{0,s}} dy}{\int_0^{y_{end}} \rho u \, dy} \tag{1}$$

where y_{end} is the upper integration limit. Figure 19 shows the calculated recovery coefficient with the three shock generator thicknesses at varying x_1. An upper limit $y_{end} = 53$ mm has been used, as this is the height of the uppermost Pitot probe sampled. In addition, the results obtained on a flat surface with a shock impinging at $x_1/a = 0.57$ have been

included as horizontal lines with no markers, ignoring the effects of boundary layer thickening when x_1/a increases.

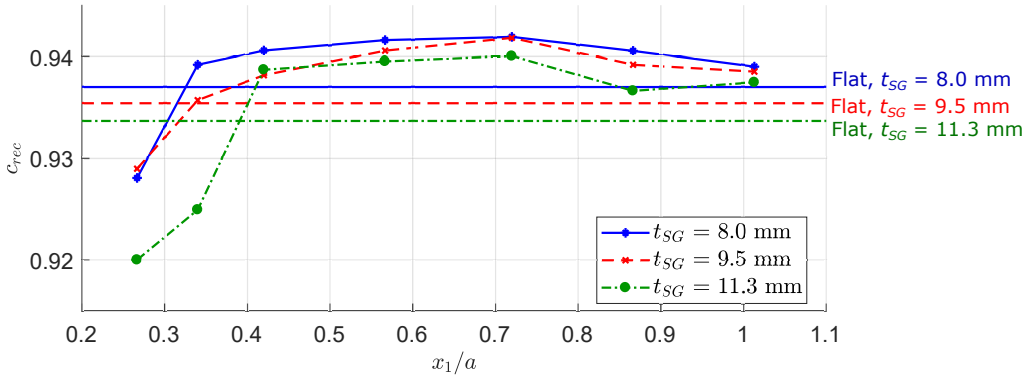

Fig. 19 Mass-weighted stagnation recovery coefficient against shock position.

Improvements in the stagnation pressure recovery are observed with respect to the flat surface case when the shock impinges in the range $0.42 \leq x_1/a \leq 1.01$, with maximum recovery occurring when the shock lies on the central region of the flexible plate ($0.57 \leq x_1/a \leq 0.72$). Reductions between 8% and 10% in the mass-averaged losses are found if this is the case, and this is true for all the SBLI–expansion distances considered.

Examination of the stagnation pressure profiles in Fig. 18 shows that stagnation pressure losses are not dominated by losses in the outer flow, where shock structures play a major role, and rather by dissipation within the boundary layer. Hence, the test cases with thinner boundary layers also provide greater recovery coefficients. In fact, comparison of Figs. 17 and 19 reveals a clear correlation, as the test cases with smaller separation bubbles also provide higher downstream stagnation pressure recovery. It is hypothesized that this is due to reduced viscous dissipation in the separation region.

In order to examine the effects of changing the integration limit y_{end}, a sensitivity study was conducted. This confirmed that the bump can provide improved stagnation pressure recovery irrespective of the integration limits used.

F. Synthesis

The experimental static pressure distributions along the centerline of the plate in Fig. 8 have shown that there exists a shock impingement location that results in maximum pressure on the plate. Tan et al. [6] hypothesized the existence of this optimum point and suggested that it could result in improved stagnation pressure downstream of the bump. Numerical simulations show that this is indeed the case, at least outside the boundary layer, as illustrated in Fig. 18.

Moreover, examining the schlieren and oil flow images for varying shock streamwise impingement positions (Figs. 5 and 12), it was noticed that a shock impinging near the front or rear of the flexible plate caused large separation bubbles and SBLI upstream influences. On the contrary, a shock impinging on some location around the mid-chord of the flexible plate resulted in a separation bubble of minimum length. These observations are further supported by the

numerical results in Fig. 17, where this minimum separation length was not only observed, but it was also significantly lower than if the bump were not present. When examining the numerical recovery coefficient in Fig. 19, it was found that, if the shock impinges on the middle of the bump, the flexible surface also provides improved stagnation pressure as compared to the flat surface case. This is due to a combination of reduced separation length (resulting in thinner boundary layers) and more efficient compression of the outer flow.

Figure 20 compares the observed flow structures at three different shock impinging positions. If the shock impinges too far upstream, as in Fig. 20(a), or too far downstream, as in 20(c), the large separation bubbles and inefficient flow compression limit the attainable total pressure recovery. The configuration in 20(b) with a shock at the mid-chord provides maximum stagnation pressure recovery. Most importantly, improvements with respect to the flat surface case are found for a range of shock impingement positions: $0.42 \leq x_1/a \leq 1.01$. This suggests that the bump could remain beneficial even for varying flow conditions.

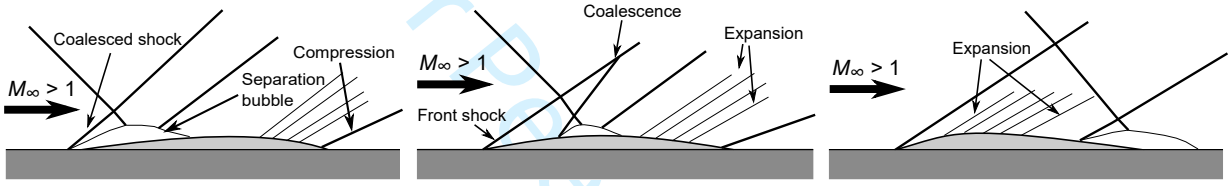

(a) Front impingement **(b) Middle impingement** **(c) Rear impingement**

Fig. 20 Schematic diagrams of SBLIs on a flexible surface at different shock impingement locations. The optimum position for maximum stagnation pressure recovery is shown in (b).

Furthermore, testing with different shock generator thicknesses has shown that these trends of (1) greater static pressure loads, (2) reduced separation length, and (3) improved stagnation recovery if the shock impinges at the mid-chord of the bump are also applicable when the SBLI–expansion distance increases. This highlights the potential application of flexible surfaces for SBLI control in supersonic inlets, where no expansion exists downstream of the shock.

V. Conclusions

This study investigated oblique shock–boundary layer interactions on a flexible panel in an $M_\infty = 2$ flow. A parametric study was conducted in the Imperial College supersonic wind tunnel, in which the effects of varying the shock impingement position and the SBLI–expansion distance were explored. In addition, two-dimensional steady simulations were used to study the effectiveness of the bump in improving downstream total pressure recovery. The computational results were validated against static and Pitot pressure experimental measurements. Numerical simulations accurately predict the main trends in the static and Pitot pressure profiles, although they consistently underpredict the SBLI pressure rise.

By moving the shock generator in the streamwise direction, inviscid shock impingement positions in the range $0.27 \leq x_1/a \leq 1.01$ have been tested. The static pressure distributions, measured along the centerline of the flexible surface, have shown that maximum static pressure is achieved when the shock impinges on the region $0.34 \leq x_1/a \leq 0.57$, with the exact location varying depending on the shock generator thickness. This maximum exists because of the combined flow compression due to plate curvature and the SBLI, before any flow re-acceleration.

Oil flow visualization was used to measure the separation length. Numerical simulations, which agree well with the experimental values, show reductions of the order of 40 % in the separation length with respect to the flat surface case if the shock impinges on the flexible plate in the range $0.34 \leq x_1/a \leq 0.87$. When the SBLI lies outside this range, a degradation in performance is observed, resulting in separation lengths up to 45 % larger than if the flexible surface were not used.

Using numerical simulations, improvements in downstream stagnation pressure recovery with respect to the flat surface case are also found for shock positions in the range $0.42 \leq x_1/a \leq 1.01$. In particular, CFD results show that the mass-averaged stagnation pressure losses can be reduced by between 8 % and 10 % if a flexible surface is used.

The effects of changing the SBLI–expansion were explored by varying the shock generator thickness between $t_{SG} = 11.3$ and 8.0 mm, while maintaining a constant tunnel aspect ratio $\mathcal{AR} = 1.25$. Experimental results show reductions in the static pressure rise when the expansion is moved closer to the SBLI, implying a weakening of the interaction. Similarly, decreasing the SBLI–expansion distance also results in a reduction in the SBLI upstream influence, as shown by schlieren images and static pressure distributions. Both oil flow and computational results show that this decrease in the upstream influence is associated with a reduction in size of the separation bubble. Furthermore, the improvements in separation length and total pressure recovery when the shock impinges on the middle of the bump were found to occur for all the shock generator thicknesses used in the simulations.

Further research is desirable to confirm whether the beneficial performance of flexible surfaces for oblique shock control holds across a wider range of shock angles and Mach numbers. Such tests would be necessary to verify the considerable potential of flexible surfaces as a passive and mechanically-simple form of shock control in next-generation supersonic inlets.

Acknowledgments

The second author would like to acknowledge the Imperial College President's PhD Scholarship Scheme, supported by EPSRC, for their support of this research. The authors wish to acknowledge Mr Dilaksan Thillaithevan for his assistance with the experimental testing.

References

[1] Hirt, S., Reich, D., and O'Connor, M., "Microramp Flow Control for Oblique Shock Interactions: Comparisons of Computational and Experimental Data," *5th Flow Control Conference*, American Institute of Aeronautics and Astronautics, 2010. doi: https://doi.org/10.2514/6.2010-4973.

[2] Giepman, R. H. M., Schrijer, F. F. J., and van Oudheusden, B. W., "Flow control of an oblique shock wave reflection with micro-ramp vortex generators: Effects of location and size," *Physics of Fluids*, Vol. 26, No. 6, 2014, p. 066101. doi:https://doi.org/10.1063/1.4881941.

[3] Zhang, Y., jun Tan, H., Sun, S., and yan Rao, C., "Control of Cowl Shock/Boundary-Layer Interaction in Hypersonic Inlets by Bump," *AIAA Journal*, Vol. 53, No. 11, 2015, pp. 3492–3496. doi:https://doi.org/10.2514/1.j053974.

[4] Brouwer, K. R., Gogulapati, A., and McNamara, J. J., "Interplay of Surface Deformation and Shock-Induced Separation in Shock/Boundary-Layer Interactions," *AIAA Journal*, Vol. 55, No. 12, 2017, pp. 4258–4273. doi:https://doi.org/10.2514/1.j056030.

[5] Zhang, Y., Tan, H.-J., Li, J.-F., and Yin, N., "Control of Cowl-Shock/Boundary-Layer Interactions by Deformable Shape-Memory Alloy Bump," *AIAA Journal*, 2018, pp. 1–10. doi:https://doi.org/10.2514/1.j057409.

[6] Tan, S. S., Bruce, P. J. K., and Gramola, M., "Oblique Shockwave Boundary Layer Interaction on a Flexible Surface," *AIAA Scitech 2019 Forum*, American Institute of Aeronautics and Astronautics, 2019. doi:https://doi.org/10.2514/6.2019-0097.

[7] Ashill, P. R., Fulker, J. L., and Shires, A., "A novel technique for controlling shock strength of laminar-flow aerofoil sections," *DGLR Bericht Part 6*, Vol. (92–01–022), 1992, pp. 175–183.

[8] Birkemeyer, J., Rosemann, H., and Stanewsky, E., "Shock control on a swept wing," *Aerospace Science and Technology*, Vol. 4, No. 3, 2000, pp. 147–156. doi:https://doi.org/10.1016/s1270-9638(00)00128-0.

[9] Bruce, P. J. K., Colliss, S., and Babinsky, H., "Three-dimensional shock control bumps: effects of geometry," *52nd Aerospace Sciences Meeting*, American Institute of Aeronautics and Astronautics, 2014. doi:https://doi.org/10.2514/6.2014-0943.

[10] Kim, S. D., "Aerodynamic Design of a Supersonic Inlet with a Parametric Bump," *Journal of Aircraft*, Vol. 46, No. 1, 2009, pp. 198–202. doi:https://doi.org/10.2514/1.37416.

[11] Bruce, P. J. K., and Colliss, S. P., "Review of research into shock control bumps," *Shock Waves*, Vol. 25, No. 5, 2014, pp. 451–471. doi:https://doi.org/10.1007/s00193-014-0533-4.

[12] Ogawa, H., Babinsky, H., Pätzold, M., and Lutz, T., "Shock-Wave/Boundary-Layer Interaction Control Using Three-Dimensional Bumps for Transonic Wings," *AIAA Journal*, Vol. 46, No. 6, 2008, pp. 1442–1452. doi:https://doi.org/10.2514/1.32049.

[13] Visbal, M., "Viscous and inviscid interactions of an oblique shock with a flexible panel," *Journal of Fluids and Structures*, Vol. 48, 2014, pp. 27–45. doi:https://doi.org/10.1016/j.jfluidstructs.2014.02.003.

[14] Jinks, E. R., Bruce, P. J. K., and Santer, M. J., "The Use of Actuated Flexible Plates for Adaptive Shock Control Bumps," *53rd AIAA Aerospace Sciences Meeting*, American Institute of Aeronautics and Astronautics, 2015. doi:https://doi.org/10.2514/6.2015-1241.

[15] Gramola, M., Bruce, P. J. K., and Santer, M. J., "FSI study of 2D adaptive shock control bumps," *AIAA Scitech 2019 Forum*, American Institute of Aeronautics and Astronautics, 2019. doi:https://doi.org/10.2514/6.2019-1845.

[16] Shinde, V., Gaitonde, D. V., and McNamara, J. J., "Control of Transitional Shock Boundary Layer Interaction using Surface Morphing," *AIAA Scitech 2019 Forum*, American Institute of Aeronautics and Astronautics, 2019. doi:https://doi.org/10.2514/6.2019-1895.

[17] Grossman, I. J., and Bruce, P. J. K., "Effect of Test Article Geometry on Shock Wave-Boundary Layer Interactions in Rectangular Intakes," *55th AIAA Aerospace Sciences Meeting*, American Institute of Aeronautics and Astronautics, 2017. doi:https://doi.org/10.2514/6.2017-0758.

[18] Hirt, S. M., "Experimental Study of Fillets to Reduce Corner Effects in an Oblique Shock-Wave/Boundary-Layer Interaction," *53rd AIAA Aerospace Sciences Meeting*, American Institute of Aeronautics and Astronautics, 2015. doi:https://doi.org/10.2514/6.2015-1239.

[19] Grossman, I. J., and Bruce, P. J. K., "Effect of Confinement on Shock Wave-Boundary Layer Interactions in Rectangular intakes," *54th AIAA Aerospace Sciences Meeting*, American Institute of Aeronautics and Astronautics, 2016. doi:https://doi.org/10.2514/6.2016-0348.

[20] Threadgill, J. A., and Bruce, P. J. K., "Unsteadiness in Shock Wave Boundary Layer Interactions across Multiple Interaction Configurations," *53rd AIAA Aerospace Sciences Meeting*, American Institute of Aeronautics and Astronautics, 2015. doi:https://doi.org/10.2514/6.2015-1977.

[21] Jinks, E. R., Bruce, P. J. K., and Santer, M. J., "Wind Tunnel Experiments with Flexible Plates in Transonic Flows," *54th AIAA Aerospace Sciences Meeting*, American Institute of Aeronautics and Astronautics, 2016. doi:https://doi.org/10.2514/6.2016-1553.

[22] Dowell, E. H., "Panel flutter - A review of the aeroelastic stability of plates and shells," *AIAA Journal*, Vol. 8, No. 3, 1970, pp. 385–399. doi:https://doi.org/10.2514/3.5680.

[23] Gramola, M., Bruce, P. J. K., and Santer, M., "Photogrammetry for accurate model deformation measurement in a supersonic wind tunnel," *Experiments in Fluids*, Vol. 60, No. 1, 2018. doi:https://doi.org/10.1007/s00348-018-2652-7.

[24] *PhotoModeler Motion*, PhotoModeler Technologies, 2019.

[25] Stamatopoulos, N., Gatos, B., Pratikakis, I., and Perantonis, S. J., "A Two-Step Dewarping of Camera Document Images," *2008 The Eighth IAPR International Workshop on Document Analysis Systems*, IEEE, 2008. doi:https://doi.org/10.1109/das.2008.40.

[26] Babinsky, H., Oorebeek, J., and Cottingham, T., "Corner effects in reflecting oblique shock-wave/boundary-layer interactions," *51st AIAA Aerospace Sciences Meeting including the New Horizons Forum and Aerospace Exposition*, American Institute of Aeronautics and Astronautics, 2013. doi:https://doi.org/10.2514/6.2013-859.

[27] Bruce, P. J. K., Burton, D. M. F., Titchener, N. A., and Babinsky, H., "Corner effect and separation in transonic channel flows," *Journal of Fluid Mechanics*, Vol. 679, 2011, pp. 247–262. doi:https://doi.org/10.1017/jfm.2011.135.

[28] *Star-CCM+*, Siemens PLM Software, 2018. Version 13.04.011.

[29] Singh, A. P., Duraisamy, K., and Pan, S., "Characterizing and Improving Predictive Accuracy in Shock-Turbulent Boundary Layer Interactions Using Data-driven Models," *55th AIAA Aerospace Sciences Meeting*, American Institute of Aeronautics and Astronautics, 2017. doi:https://doi.org/10.2514/6.2017-0314.

[30] Bardina, J. E., Huang, P. G., and Coakley, T. J., "Turbulence modeling validation, testing, and development," NASA Technical Memorandum 110446, NASA, 1997.

[31] Schlichting, H., and Gersten, K., *Boundary-Layer Theory*, Springer-Verlag GmbH, 2016.

[32] Anderson, J. D., *Fundamentals of Aerodynamics*, 5th ed., McGraw-Hill Education Ltd, 2010.

[33] Benek, J., "Lessons Learned from the 2010 AIAA Shock Boundary Layer Interaction Prediction Workshop," *28th AIAA Applied Aerodynamics Conference*, American Institute of Aeronautics and Astronautics, 2010. doi:https://doi.org/10.2514/6.2010-4825.

Oblique shock control with steady flexible panels

Nicolas Gomez-Vega*, Michela Gramola†, and Paul J. K. Bruce‡
Department of Aeronautics, Imperial College London, SW7 2AZ, United Kingdom

Flexible panels deforming under pressure loads have been suggested as a passive form of adaptive oblique shock control. This study investigates oblique shock–boundary layer interactions on a steady flexible panel in a Mach 2.0 flow. Experiments were performed in the Imperial College supersonic wind tunnel, where shock generators were used to produce an oblique shock followed by a corner expansion. A parametric study was conducted, exploring different shock impingement positions and shock–expansion distances. The steady aero-structural response is studied using schlieren photography, static pressure distributions, photogrammetry measurements, and surface oil flow visualisation. Two-dimensional numerical simulations were performed to assess the effects of the flexible panel on downstream total pressure recovery. These were validated against experimental wall pressure distributions and measurements from a Pitot rake. Results show reductions in both separation length (of up to 40 %) and stagnation pressure losses (of up to 10 %) if the flexible plate is used. These improvements occur for a range of shock positions spanning approximately 50 % of the panel length and for all the shock–expansion distances considered. A model that captures the flow physics responsible for these trends is proposed. The results highlight the potential of flexible panels for practical oblique shock control.

Nomenclature

a	=	plate length, mm
$\mathcal{AR}$	=	tunnel aspect ratio
c_f	=	skin-friction coefficient
l	=	mesh target surface size, mm
L_{int}	=	interaction length, mm
L_{sep}	=	separation length, mm
P_a	=	atmospheric pressure, Pa
P_c	=	cavity pressure, Pa

*Graduate, Department of Aeronautics, Imperial College London
†PhD Candidate, Department of Aeronautics, Imperial College London, AIAA Student Member
‡Senior Lecturer, Department of Aeronautics, Imperial College London, AIAA Senior Member

P_p = Pitot pressure, Pa

P_0 = stagnation pressure, Pa

$P_{0,s}$ = settling chamber stagnation pressure, Pa

t_{SG} = shock generator thickness, mm

u = flow velocity, m s^{-1}

w = plate deflection, mm

x_e = impingement point of the expansion's head, mm

x_r = re-attachment point, mm

x_s = separation point, mm

x_{SG} = shock generator streamwise location, mm

x_1 = inviscid shock impingement point, mm

y^+ = dimensionless wall distance

δ = boundary layer thickness, mm

θ = flow deflection, deg

ρ = density, kg m^{-3}

I. Introduction

The main function of a supersonic engine inlet is to decelerate the flow to subsonic conditions in the most efficient way possible, without great losses in stagnation pressure. A common strategy for this involves the generation of oblique shock structures, reflecting off the internal surfaces of the inlet. As these shocks meet the boundary layers growing along the surfaces, shock–boundary layer interactions (SBLIs) develop. These often cause undesirable separation and unsteadiness, leading to stagnation pressure losses and lower efficiency. Therefore, it is not surprising that oblique SBLIs have become a target for flow control [1–6].

A promising method for SBLI control are shock control bumps, which are contoured protrusions on aerodynamic surfaces. These have been investigated for applications ranging from transonic wings [7–9] to engine inlets [3, 10]. The potential of shock control bumps for normal shock control has been widely demonstrated despite their sensitivity to shock position and changes in flow conditions [11]. If the normal shock impinges away from its design position, additional shock and expansion structures develop, leading to worsened performance [12].

Aircraft and engine components are made of relatively flexible materials, which may deform under pressure loads. The interplay between surface deformations and the SBLI properties, an example of fluid–structure interaction ~~(FSI)~~, has become a subject of recent research interest in the context of adaptive shock control. Some groups have investigated dynamic shock control via vibrating surfaces [4, 13], while others have focused on static control with steady contoured

surfaces [6, 14, 15]. In this sense, steady flexible panels have been suggested as a simple form of passive oblique shock control, in a manner analogous to shock control bumps for transonic applications [6]. Previous studies on oblique SBLIs on flexible surfaces have highlighted potential reductions in the size of the separation region with increasing surface curvature [4, 6], a first step towards flow control.

For flexible panels to realize their potential as a practical means of oblique shock control in engine inlets, they must provide reduced total pressure losses. Some numerical investigations [5, 16] have suggested that contoured surfaces can lead to improved downstream stagnation pressure. No experimental confirmation of this currently exists, due to the technical challenges in measuring accurate stagnation pressure profiles in supersonic flows, particularly within the boundary layer. Nevertheless, the wall pressure distributions in Tan et al. [6] show that, for some shock positions, flexible panels can lead to more efficient flow compression upstream of the impinging oblique shock, potentially weakening the interaction and reducing losses.

Oblique SBLIs are also common in aircraft component–component interactions. For example, a supersonic aircraft with externally-mounted stores (such as fuel tanks or missiles) would experience an oblique shock impinging on the fuselage. In these cases, the incident shock is often followed by an expansion, which counters many of the effects of the SBLI by imposing a favourable pressure gradient. A simple way to produce an oblique shock in a wind tunnel is with a wedge-shaped plate, often referred to as a “shock generator". By necessity, these devices also introduce an expansion fan, as they must return the flow parallel to the freestream some distance downstream of the compression. Studies on oblique SBLIs often try to decouple these effects, either by increasing the SBLI–expansion distance [17] or by modifying the shock generator geometry [18]. The study of how this expansion affects flow properties is of interest, since component–component interactions in real aircraft usually produce similar shock–expansion structures. Studies on flat surfaces [17, 19] have found reductions in the separation length as the expansion is brought closer to the SBLI. Nevertheless, this interplay has not been explored on flexible surfaces thus far.

In this context, this study investigates the suitability of using steady flexible surfaces deforming under pressure loads for static oblique shock control. Experiments are conducted at Mach 2.0 in the Imperial College supersonic wind tunnel on a thin aluminium plate, using shock generators with 10° wedge angles. By varying the shock generator thickness, the effect of changing the distance between the shock and the expansion impingement points is studied. Particular focus is given to small SBLI–expansion distances, typical of those in aircraft component interactions. Similarly, the effects of changing the streamwise shock impingement point, at constant SBLI–expansion distance, are also explored. The experimental setup is described in Sec. II, while the results are presented and discussed in Sec. IV.

The experimental setup did not allow the reconstruction of the downstream total pressure profile. In order to overcome this, all experimental test cases have been replicated in two-dimensional Reynolds-averaged Navier Stokes (RANS) simulations in order to obtain downstream total pressure profiles. In these, the experimental wall profiles measured using photogrammetry are imposed as solid boundaries. Further details regarding the models and assumptions

in the numerical simulations are examined in Sec. III. Finally, the numerical results are validated and discussed in Sec. IV.E.

II. Experimental Methods

Experiments were performed in the Imperial College London (ICL) supersonic wind tunnel, a blow-down facility supplied with dry air from tanks pressurized to 2.7 MPa. The tanks provide sufficient compressed air for run-times of approximately 40 s, followed by a recharging time of several hours. Flow conditions at the settling chamber are controlled by a pneumatic valve that regulates stagnation pressure using a PID controller. For the present investigation, the tunnel was fitted with a Mach 2.0 supersonic nozzle. The flow conditions in the wind tunnel were characterized by Threadgill & Bruce [20], who reported an incoming boundary layer thickness $\delta = 5.87$ mm just upstream of the region of interest in this study.

The flexible plate was installed in the test section of the tunnel, which has a square cross-section and dimensions 727 mm long × 150 mm wide × 150 mm tall. A schematic diagram of the test section, along with the fitted equipment and the coordinate system, is shown in Fig. 1.

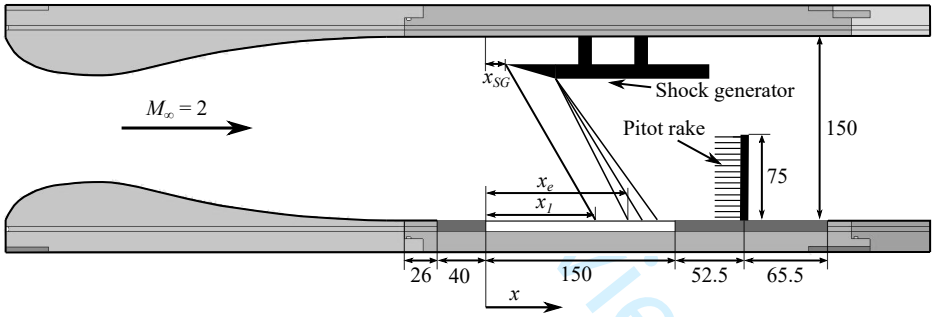

Fig. 1 Wind tunnel nozzle and test section, labeled with the relevant geometric parameters. Dimensions in mm.

Oblique shocks in the test section were produced using shock generators, which are wedge-shaped plates as shown in Fig. 1. As the flow turns around the convex corner on the underside of the shock generator, an expansion develops. All the shock generators in this study had a spanwise width of 148 mm and a wedge angle of $\theta = 10°$. The shock generators were attached to the top of the tunnel by two actuated mounts. The points x_1 and x_e in Fig. 1 respectively correspond to the inviscid shock and expansion impingement points on an undeformed flat plate.

The flexible plate assembly is made of the aluminum alloy Al 7075-T6 and has the same basic design as those described in Jinks et al. [21] and Tan et al. [6]. The plate was designed against flutter using the criterion in Dowell [22]. It contains a thin panel of length $a = 150$ mm, ~~width-to-length ratio of 1~~ width 149 mm, and thickness $h = 0.6$ mm. The two longitudinal ends of the flexible plate are clamped to ~~the~~ supports, while the two sides are free. A 0.5 mm gap exists between either side of the plate and the wind tunnel's walls. Each support was bolted to the wind tunnel floor at four

points. Further details regarding the plate design and mounting may be found in the Supplemental Materials The flexible portion of the plate contains a total of 15 pressure tappings placed along the centerline, with the upstream support containing two additional tappings. Following the setup in Tan et al. [6], three aluminum spacers, each of thickness 0.4 mm, were slotted underneath the plate assembly to constrain end displacements.

Underneath the flexible panel, there sits a small chamber, known as the "cavity", sealed at all points except for the two sides of the plate and for the hole drilled for the Pitot rake tubes, which is itself partially blocked by these tubes. Since the mean flow is not isolated from the cavity, there is some leakage of air from the cavity into the flow ~~is expected~~. The difference between the pressures in the cavity (referred to as "cavity pressure", P_c) and in the flow is what drives plate deformations.

The plate assembly is fitted with a vertical Pitot rake positioned downstream of the flexible portion as shown in Fig. 1. The rake has a total of 15 Pitot probes for a total height of 75 mm, although only the 11 lowest ones were sampled. The probes are 5 mm apart, with the first one placed 3 mm above the surface. Since the bulk flow downstream of the plate is still supersonic, the pressure measured by these probes ("Pitot pressure", P_p), is not the same as the stagnation pressure. The Pitot rake did not contain static pressure tappings, and therefore, the experimental stagnation pressure could not be calculated. Due to this, numerical simulations were used to estimate the downstream total pressure, and their calculated Pitot pressures were compared to the experimental ones for verification. Pressure measurements were taken using a Netscanner pressure transducer, sampling at 100 Hz. Pressure data was sampled for a period of 5 s for each test case once the settling chamber pressure had reached the steady-state. Moreover, the standard deviation was recorded for each measurement, and this was used as a measure of experimental errors.

Schlieren photography was employed to observe the flow structure above the flexible panel. A Z-type configuration was used, ~~with two 200 mm diameter concave mirrors with a focal length of 1200 mm~~ in which light from a Thorlabs MCWHL5 LED point source with a Thorlabs LEDD1B driver was reflected on two 200 mm diameter concave mirrors with a focal length of 1200 mm. The light was focused on an aperture with a vertical knife-edge, blocking the right-half of the light. Schlieren images were recorded with a Phantom v641 high-speed camera.

Point-tracking photogrammetry was used to reconstruct the 3D bump profile. Following the work of Gramola et al. [23], eighty 12-bit coded targets, each of thickness 20 µm, were attached to the surface of the plate. The motion of these targets was recorded using four synchronized Phantom Miro 310 cameras, placed at different angles around the viewing panels of the working section. All the cameras had a resolution of 1280×800 pixels and recorded at the same frequency as the pressure transducers (100 Hz). Further details regarding the setup, calibration and post-processing may be found in Gramola et al. [23]. For every run, a photograph was extracted from each of the four cameras once the plate deformations were steady. These images were subsequently processed using the commercial software *PhotoModeler Motion* [24], allowing the reconstruction of the 3D bump profile.

The separation region was observed using surface oil flow visualisation. For these experiments, the photogrammetry

targets were removed. An oil mixture was injected onto the surface of the tunnel floor through two holes in the plate assembly, which are 60 mm apart and 8 mm downstream of the front of the panel. The oil was a mixture of oleic acid, titanium dioxide and kerosene, in the following proportions: for every 17 g of kerosene, 10 g of titanium dioxide and 11 drops of oleic acid. Oil motion was filmed through the sidewall viewing panels using one of the photogrammetry cameras. Since oil flow images were taken at an angle, a dewarping process was necessary to correct for the effects of perspective and plate deformations. For this purpose, the geometric method in Stamatopoulos et al. [25] was implemented, consisting in mapping pixels on a curved surface to a 2D rectangular area. Once the dewarped images were obtained, these were used to produce streakline schematic diagrams.

A parametric study was performed by testing several shock and expansion impingement points. A parameter affecting the SBLI–expansion distance is the tunnel aspect ratio $\mathcal{AR}$, which is defined here as the effective width-to-height ratio of the wind tunnel test section, ~~although alternative definitions exist~~ with the height being measured from the wind tunnel floor to the tip of the shock generator. Alternative definitions exist; for example, some authors [26, 27] define an unrelated "viscous aspect ratio". A high aspect ratio, with a shock generator close to the floor, would provide larger SBLI–expansion distances; however, it would also interfere with the photogrammetry equipment, covering the targets, and could cause tunnel unstart. In order to prevent this, experiments were conducted at a constant aspect ratio of $\mathcal{AR} = 1.25$. This choice provides an adequate maximum SBLI–expansion distance (17 mm) whilst ensuring that the photogrammetry targets are not covered. Because of this choice, the SBLI–expansion distance was varied using shock generators of different thicknesses.

A total of 21 test cases were examined using three different shock generators thicknesses ($t_{SG} = 11.3$ mm, 9.5 mm and 8.0 mm) with a constant wedge angle $\theta = 10°$. The shock generator streamwise location was varied between tests to obtain seven streamwise shock positions, in the range $0.27 \leq x_1/a \leq 1.01$, for each shock generator thickness. The different shock generator thicknesses provide three different SBLI–expansion distances $x_e - x_1$ (following the notation in Fig. 1) to be tested: 17, 8 and 1 mm. It should be noted that, in calculating these distances, it was assumed that the expansion crosses the reflected shock unhindered as suggested by Grossman & Bruce [17]. Similarly, the effects of plate deformations, which are not known in advance, on x_1 and x_e were also ignored. All test cases were conducted with a settling chamber pressure ratio $P_{0,s}/P_a = 1.80$, which was expected to provide fully supersonic flow in the test section.

Moreover, six additional test cases were conducted with the oil flow visualisation setup. These explore the impact of shock streamwise position and shock generator thickness on flow separation.

III. Numerical Simulations

A numerical investigation was conducted using the commercial Computational Fluid Dynamics (CFD) software *Star-CCM+* [28] in order to quantify the effects of the flexible plate on downstream total pressure recovery. Fully-turbulent, steady simulations were performed in a two-dimensional domain to reduce the computational costs. In these,

the RANS equations were solved via the finite volume method using a coupled flow ~~solver~~ model, which solves the mass and momentum equations simultaneously. Air was assumed to behave as a calorically perfect gas, with a viscosity governed by Sutherland's law.

A turbulence model was used to close the RANS equations. Popular choices for numerical simulations of flows with shock–boundary layer interactions include the one-equation Spalart-Allmaras model [15, 29], and the two-equation Menter's shear-stress transport (SST) k-ω model [3–5]. Among these, the Menter SST k-ω model was selected due to its superior performance in flows with strong adverse pressure gradients and separation [4, 30].

The main boundary conditions in the simulations are the inlet conditions (pressure and temperature) and velocity profile, and the outlet pressure. The inlet velocity profile was calculated with a one-seventh power law, given by Eq. (20.6) in Schlichting [31], using the boundary layer parameters measured by Threadgill & Bruce [20] for the ICL supersonic wind tunnel. This provides an incompressible shape factor $H = 1.286$, which matches the value reported by Threadgill & Bruce [20], $H = 1.28$. Both the inlet and outlet static pressures are set constant and equal to $P_\infty = 23.3\,\text{kPa}$, which is the static pressure corresponding to an $M_\infty = 2$ flow with $P_0 = 1.8\,\text{atm}$.

The computational domain is shown in Fig. 2. All walls are assumed to be adiabatic, and the bump profiles for each simulation are obtained from photogrammetry measurements.

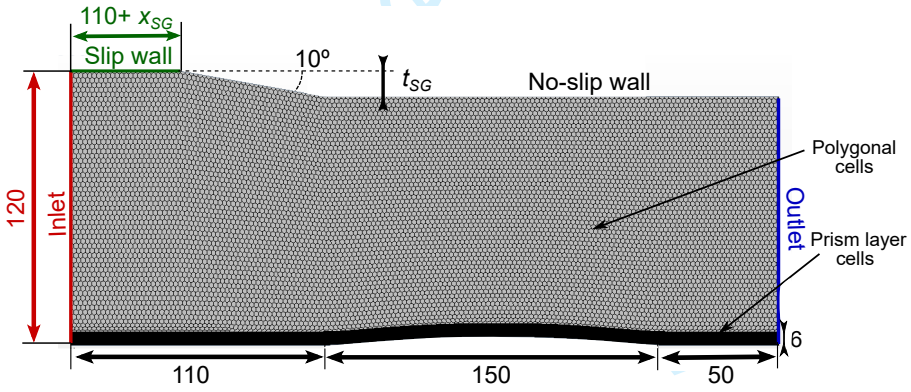

Fig. 2 Computational domain, labeled with dimensions and boundary conditions. Dimensions in mm.

Due to the curvature of the flexible plate, a polygonal mesher was selected. In addition, a prism layer mesh, with quadrilateral cells of high aspect ratio, was used along the bottom boundary to better capture the boundary layer profile. The near-wall cell thickness was selected so that $y^+ \approx 1$. To ensure an adequate resolution of the boundary layer, a total of 150 prism cells were used in the wall-normal direction for a total prism layer thickness of 6 mm, which is slightly larger than the initial boundary layer height, $\delta = 5.8\,\text{mm}$.

A mesh refinement study was conducted in order to determine the target surface size of the polygonal cells l, which is the reference edge length that the mesher aims to achieve. The study was conducted on a computational domain similar to the one in Fig. 2, but with a flat bottom boundary. Fig. 3 shows the skin-friction coefficient distributions

predicted by each of the different meshes. Some differences in the skin friction distributions can be seen as the mesh is refined from $l = 2$ mm to $l = 0.3$ mm; whereas further refining with cell sizes smaller than $l = 0.3$ mm only result in marginal changes, indicating convergence. Based on the plots in Fig. 3, the $l = 0.2$ mm mesh has been selected, as this provides an adequate prediction of the converged skin-friction distribution at a lower cost than the most refined mesh. This choice of cell size results in meshes of the order of 1 million cells; however, the exact number of cells varies as the shock generator position is changed. A sample mesh is shown in Fig. 2, where a coarser mesh is presented for clarity.

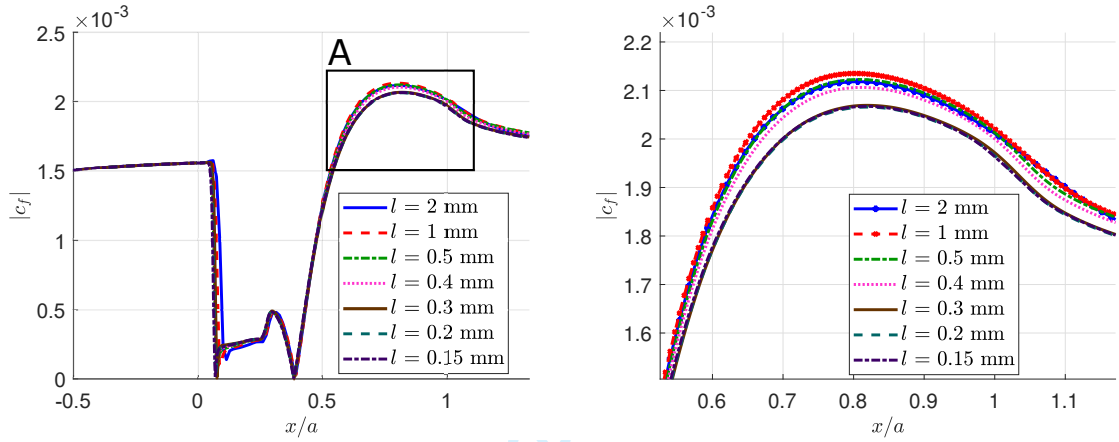

(a) Skin-friction distribution **(b) Detailed view of region A**

Fig. 3 Skin-friction coefficient distributions for different cell sizes.

In order to quantify the effects of the flexible plate on downstream stagnation pressure, all the experimental test cases were simulated. To provide baseline results, three additional simulations were conducted on a flat surface, one for each shock generator thickness.

IV. Results

All streamwise distances in this study are measured with respect to the front (leading edge) of the flexible panel, where $x = 0$ as defined in Fig. 1. Similarly, the experimental test cases are identified according to their shock generator thickness t_{SG} and their inviscid shock impingement point normalized by the plate length, x_1/a. Cavity pressure was approximately constant during a run and was found to vary in the range ~~$0.28 \leq P_c/P_{0,s} \leq 0.36$~~ $0.27 \leq P_c/P_{0,s} \leq 0.35$ across different test cases. The cavity pressure measured during each test is shown in the Supplemental materials.

A. Flow morphology

The flow morphology of an SBLI on a flexible panel is different from that on a flat surface, with plate curvature introducing additional shocks and expansions. A typical schlieren image, obtained with the flexible assembly, is shown in Fig. 4, and has been labeled with shock and flow structures that are common to all test cases.

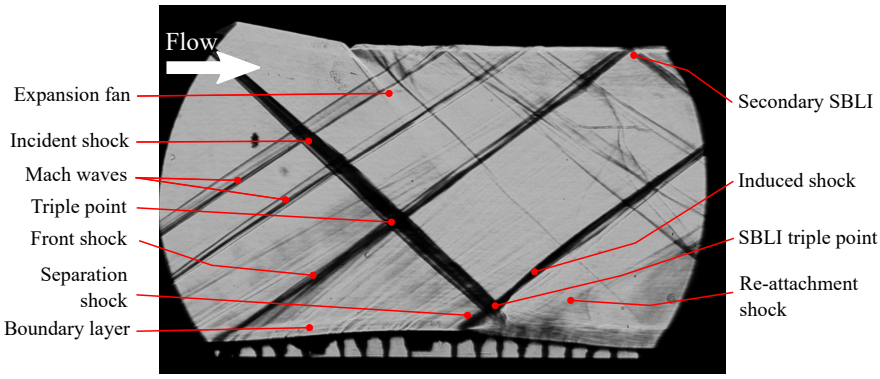

Fig. 4 Schlieren image corresponding to the t_{SG} = 11.3 mm, x_1/a = 0.87 test case, labeled with the main flow structures

The presence of the deflected flexible panel results in the formation of a shock at the front of the bump, labeled as the "front shock" in Fig. 4. This shock imposes an adverse pressure gradient but is not strong enough to cause boundary layer separation. The front shock intersects the incident shock at a downstream position, giving rise to an additional triple point, which is the intersection point itself. Moreover, a secondary, weaker SBLI can also be seen at the point where the front shock is incident on the shock generator. The expansion that forms around the convex corner on the lower side of the shock generator has also been labeled in Fig. 4, although this is barely visible due to the chosen knife-edge configuration.

The thickness of a shock wave should be of the same order as the molecule's mean free path [32]. The apparent thickness of the shocks in Fig. 4 is attributed to variations in flow conditions across the span of the tunnel, including the sidewall boundary layers.

1. Effect of changing shock impingement point

As the shock generator is moved downstream, some changes in the flow structures can be observed. These are illustrated in Fig. 5, which shows a comparison of schlieren images taken with different streamwise shock positions.

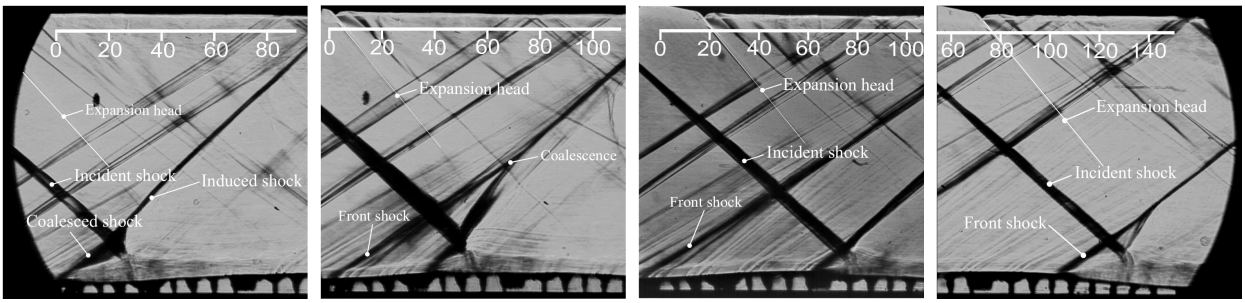

(a) x_1/a = 0.34 **(b) x_1/a = 0.57** **(c) x_1/a = 0.72** **(d) x_1/a = 1.01**

Fig. 5 Schlieren images obtained at four shock generator streamwise positions, with a constant t_{SG} = 11.3 mm shock generator. Only a portion of the images is shown. Scales in mm.

When the shock impinges near the leading edge of the flexible panel, a large separation bubble with a high upstream influence develops, as shown in Fig. 5(a). The front shock associated with concave curvature at the front of the panel and the SBLI separation shock coalesce into a single, strong shock. As the shock generator is moved downstream, the front and separation shocks split, and an independent (smaller) SBLI becomes visible; however, the front shock and the SBLI's induced shock still coalesce further downstream, as shown in 5(b). This phenomenon had been previously observed by Tan et al. [6], who referred to the resulting structure as a "tilted λ-shock". When the shock impingement point is moved further downstream, this shock coalescence is no longer observed, as seen in 5(c) and 5(d). If the shock impinges far downstream, as in 5(d), a large SBLI with a high upstream influence is observed.

2. Effect of changing shock generator thickness

The distance between the shock and the shock generator's expansion fan depends on the shock generator thickness, with thinner shock generators leading to smaller SBLI–expansion distances. The effect of varying the shock generator thickness on the flow structures, whilst maintaining the same shock generator streamwise position, is shown in Fig. 6.

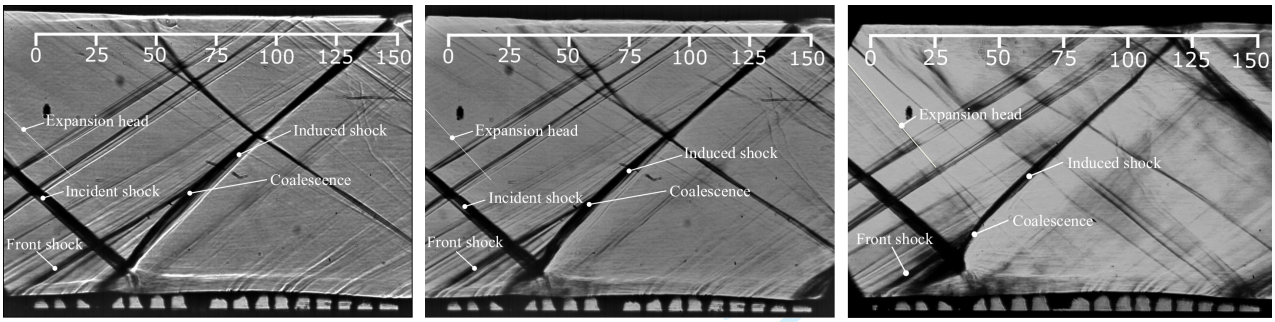

(a) t_{SG} = 8.0 mm **(b) t_{SG} = 9.5 mm** **(c) t_{SG} = 11.3 mm**

Fig. 6 Schlieren images obtained with shock generators of different thicknesses at the same streamwise position x_1/a = 0.42

~~Fig.~~Figure 6 shows that, as the expansion fan is moved further away from the SBLI, the size of the SBLI increases. This is consistent with the results of previous experiments on a flat surface by Grossman & Bruce [17]. The vertical position of the SBLI's triple point is also found to increase with increasing SBLI–expansion distance. These changes in SBLI structure are related to changes in shock-induced separation, as will be explored in Sec. IV.D.

3. Interaction lengths

In addition to providing means to visualise flow structures, the schlieren images can also be used to estimate the interaction length L_{int}, which is the upstream distance across which the shock pressure rise is smeared. In this study, the interaction length has been measured as shown in Fig. 7(a). The pixel measurement method introduces uncertainty in the interaction length measurements. This has been estimated from the schlieren images to be approximately ±1 mm.

Additional errors are caused by non-negligible shock thicknesses and optical distortion within the boundary layer; however, these have not been quantified.

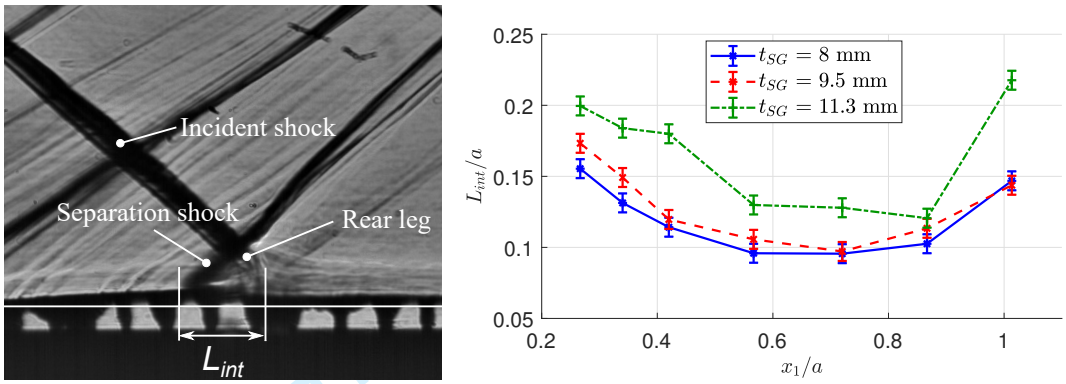

(a) Definition **(b) Interaction length plot**

Fig. 7 (a) Interaction length definition, and (b) measured interaction lengths against normalised inviscid shock impingement point.

The measured interaction lengths are plotted against the inviscid shock impingement point in Fig. 7(b). The same trend is observed for all shock generator thicknesses: as the shock impingement point moves downstream, the interaction length decreases until it reaches a minimum when the shock impinges on the downstream half of the plate, before increasing again when the shock impinges near the trailing edge. Since the interaction length is related to the size of the separation bubble, the results in Fig. 7(b) suggest that smaller separation regions could be obtained if the shock impinges on the middle region of the bump. Moreover, a reduction in the upstream influence is consistently observed when the shock generator thickness is decreased.

B. Static pressure distributions

Static pressure distributions were measured using 17 static pressure tappings placed along the centerline of the flexible plate and of the upstream mounting block. Pressure data has been time-averaged over a period of 5 s.

1. Effect of shock impingement point

The static pressure distributions obtained with the $t_{SG} = 9.5$ mm shock generator are shown in Fig. 8 and have been normalized by the settling chamber stagnation pressure $P_{0,s}$. The pressure distributions obtained with the remaining shock generators share the main trends in Fig. 8.

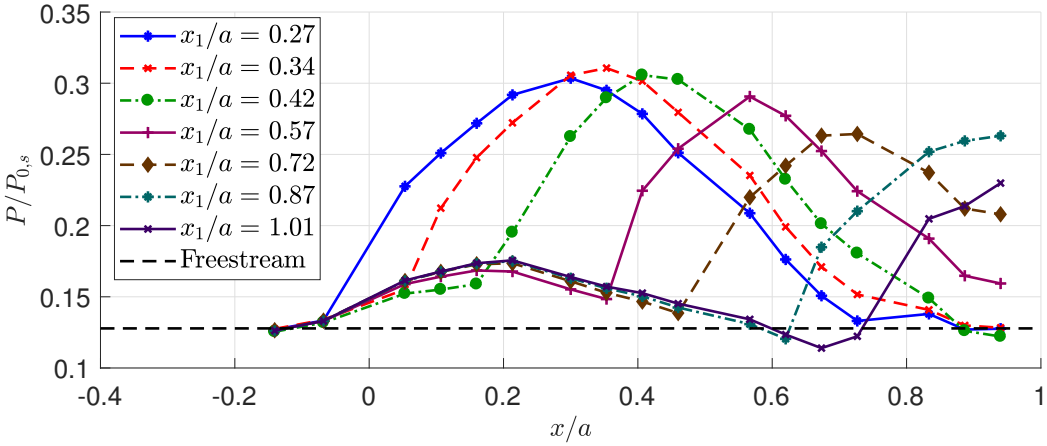

Fig. 8 Normalized static pressure distributions along the plate's centerline at varying shock impingement points, corresponding to the t_{SG} = 9.5 mm test cases.

Upstream of the flexible plate, all pressure distributions lie close to the isentropic pressure ratio at $M_\infty = 2$, which is shown as a black dashed line in Fig. 8.

A critical factor affecting the pressure distributions is surface curvature, d^2w/dx^2, which in a supersonic flow is related to the pressure gradient. In the downstream direction, pressure initially varies due to ~~the curvature of the flexible plate~~ plate bending, followed by a large pressure rise as a result of the impinging shock. The initial pressure rise due to plate ~~curvature~~ bending can be seen to varying extents in all shock streamwise positions x_1, but it is more noticeable when the shock impinges near the trailing edge of the plate. The point of maximum pressure solely due to plate deformation does not correspond to the bump's peak; instead, maximum static pressure (ignoring the shock) is reached when plate curvature as seen by the flow changes sign from concave to convex.

The SBLI pressure rise occurs upstream of the ideal inviscid shock impingement point, as a result of the shock smearing due to the interaction. After the initial sharp SBLI pressure rise, pressure continues to increase until it reaches a maximum and then decreases. This decrease in static pressure (a favourable pressure gradient) occurs because of two factors: the shock generator expansion and the negative plate curvature. The flow would be expected to re-attach in this region of favourable pressure gradient; hence, the distance between the pressure rise due to the shock and the pressure peak may be taken as a crude indicator of the separation length.

Previous investigations on the effect of the shock streamwise positions by Tan et al. [6] hypothesized the existence of a streamwise shock impingement point that would result in maximum static pressure on the plate. Furthermore, they also suggested that this would translate into improved downstream total pressure recovery due to shock weakening upstream of the SBLI. As seen in Fig. 8, this maximum static pressure indeed exists. For the t_{SG} = 9.5 mm shock generator, it corresponds to the $x_1/a = 0.34$ case, although this changes in the range $0.34 \leq x_1/a \leq 0.57$ when other shock generators are used. This maximum in the static pressure distributions occurs when the shock impinges on the

bump near the point of zero plate curvature, i.e. where there is a peak in pressure rise due to the bump shape alone. As a result, the flow undergoes a continuous compression due firstly to the bump, and subsequently the SBLI. When the shock is further downstream, re-expansion due to negative plate curvature reduces the maximum post-shock static pressure.

2. Effect of SBLI–expansion distance

When the expansion is moved closer to the SBLI, some changes in the static pressure distributions are anticipated since the expansion imposes a favourable pressure gradient. The effect of changing the shock generator thickness on the static pressures is shown in Fig. 9. Four subfigures are included, corresponding to different shock streamwise positions.

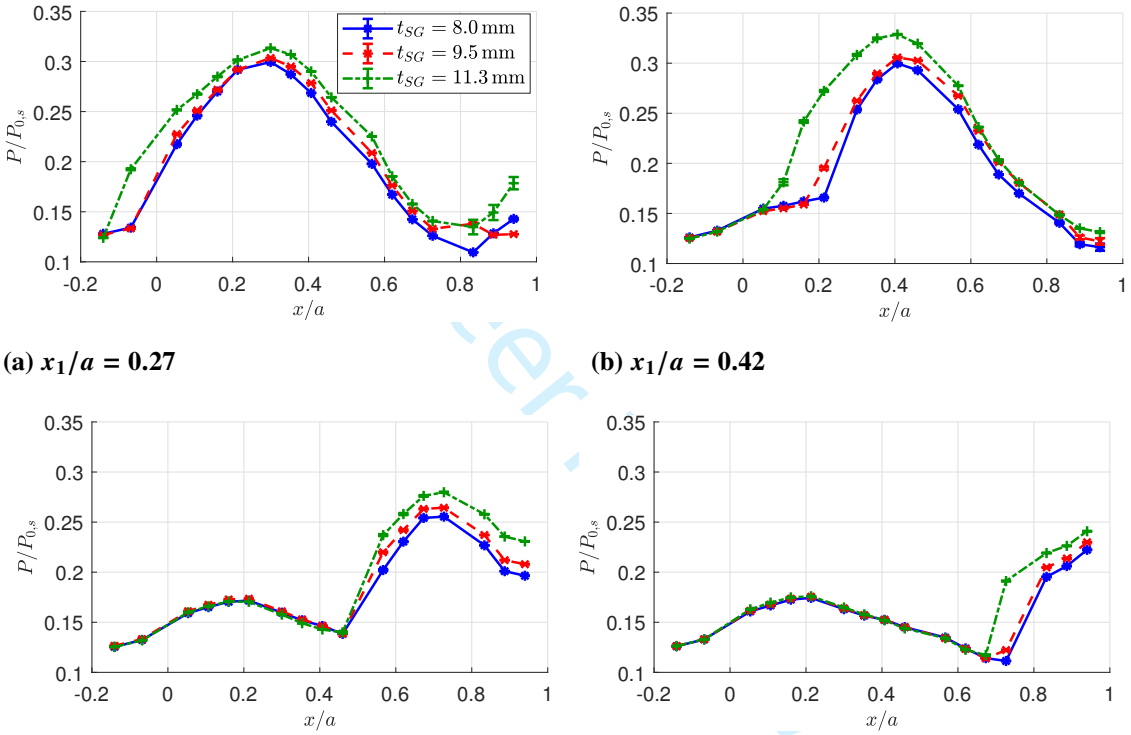

(a) $x_1/a = 0.27$ **(b) $x_1/a = 0.42$**

(c) $x_1/a = 0.72$ **(d) $x_1/a = 1.01$**

Fig. 9 Normalized static pressure distributions along the plate's centerline for changing shock generator thicknesses at four shock impingement points. Error bars represent one standard deviation.

Firstly, an increase in the SBLI strength is seen as the expansion is moved away from the shock, as shown by the greater post-shock static pressures. In addition, the SBLI pressure rise occurs further upstream as t_{SG} increases, implying greater interaction lengths. A similar trend had been previously observed by Grossman & Bruce [17] on flat surfaces. Overall, these increases in pressure and upstream influence with shock generator thickness are in line with the observations in Fig. 6, where larger interaction lengths were seen in the schlieren images with increasing SBLI–expansion distance. Upstream of the SBLI pressure rise, the pressure distributions are almost identical for all three shock generator thicknesses, suggesting that these pressure differences only result in marginally different plate

profiles.

C. Plate deformations

Using photogrammetry, the three-dimensional plate deformations have been extracted at the locations of the photogrammetry targets. Plate deformations were found to be steady once the starting shock was swallowed, and no vibrations were recorded. A sample 3D plate profile is shown in Fig. 10, where the detected positions of the coded targets are indicated with blue markers.

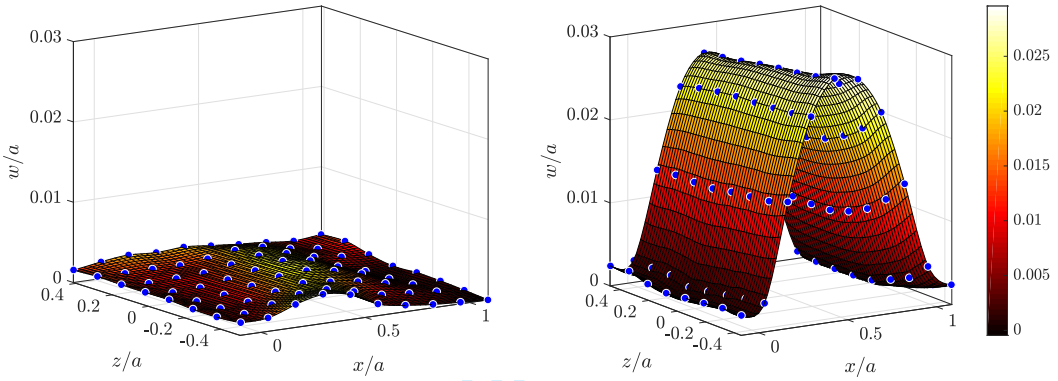

(a) Wind-off **(b) Wind-on**

Fig. 10 Sample three-dimensional plate profiles, corresponding to the $t_{SG} = 11.3$ mm, $x_1/a = 0.72$ test case. Deformations are interpolated with thin-plate smoothing splines.

Some three-dimensionality in the initial bump profile can be seen in Fig. 10(a); however, the maximum deformations are of the order of 0.5 mm, and are small compared to the wind-on deflections. These static deformations are caused by small stresses introduced by the mounting procedure. The wind-on profile in Fig. 10(b) is approximately two-dimensional, showing only small spanwise variations. Because of this, only the spanwise-averaged deformations will be considered in subsequent sections. Nevertheless, the profile in Fig. 10(b) does exhibit some degree of three-dimensionality, with slightly higher deflections near the two free ends of the plate.

The changes in static pressure due to different shock impingement points affect plate deformations. The spanwise-averaged plate profiles corresponding to the $t_{SG} = 8.0$ mm and $t_{SG} = 9.5$ mm test cases are shown in Fig. 11.

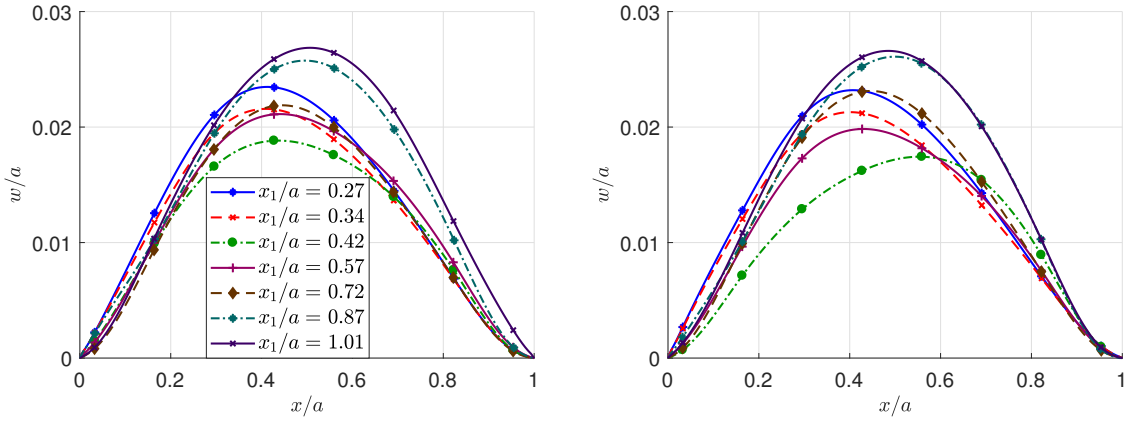

(a) t_{SG} = 8.0 mm **(b) t_{SG} = 9.5 mm**

Fig. 11 Spanwise-averaged plate deformations for varying shock impingement position, interpolated with thin-plate interpolation splines. Markers indicate the streamwise locations of the photogrammetry targets.

Plate profiles are found to change significantly with shock position. Fig. 11 shows that there is a minimum in maximum plate deflection for $x_1/a = 0.42$, while this increases for shock locations upstream and downstream of this position. ~~Plate deflections depend on the pressure difference between the freestream and the cavity; hence, the trend in Fig. 11 is consistent with the static pressure distributions in Fig. 8.~~

D. Oil flow visualisation

Surface oil flow visualisation has been used to observe the topology of the separation region by injecting oil into the boundary layer at two spanwise stations. Some representative oil flow frames are shown in Fig. 12 for different streamwise shock impingement positions. In order to aid visualisation, the contrast in these images has been modified via histogram equalisation and streaklines have been added. All figures have been marked with the streamwise and spanwise extents of the separation regions.

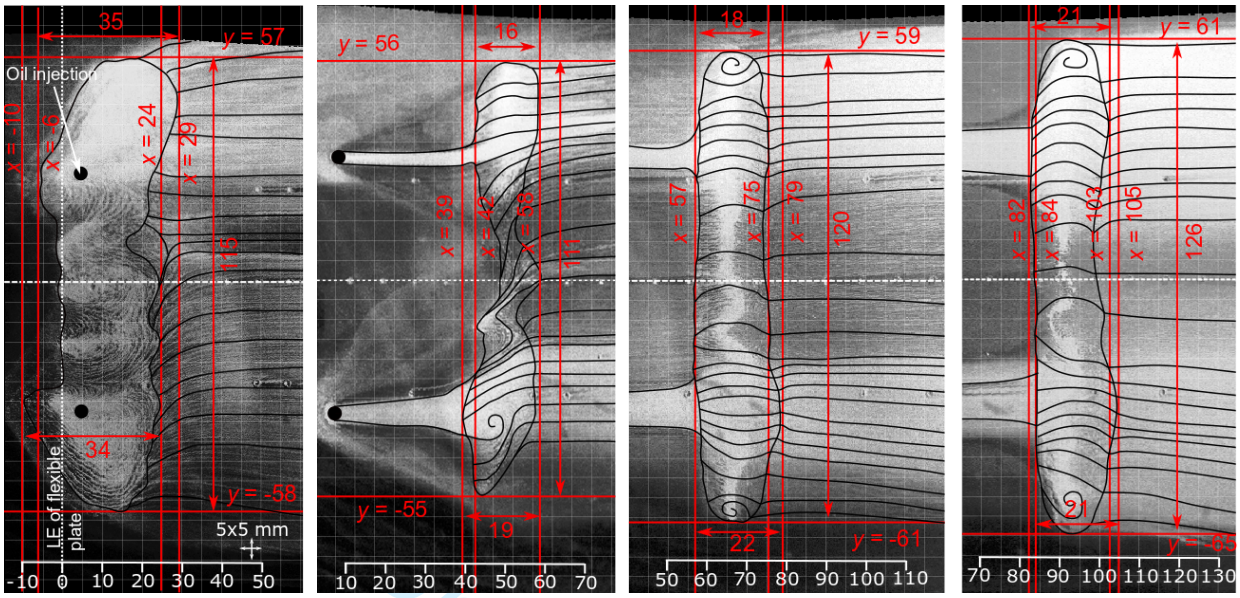

(a) $x_1/a = 0.27$ **(b)** $x_1/a = 0.42$ **(c)** $x_1/a = 0.57$ **(d)** $x_1/a = 0.72$

Fig. 12 Oil flow visualisation images for varying shock impingement point, with a constant $t_{SG} = 8.0$ mm. Streakline schematics are superimposed.

All the images in Fig. 12 display a similar trend: most of the oil is concentrated in two distinct separation cells, connected via a thinner region of cross-flow. This is, however, expected as the oil is injected at two spanwise locations. When the shock impinges near the front of the bump, such as in Fig. 12(a), a large separation bubble is formed.The flowfield in Fig. 12(a) should be interpreted with some caution relative to the other test cases since the oil was injected directly into the separation bubble and the impact of this on the separation region is unknown.

The separation bubble in Fig. 12(a) is large, with a length $L_{sep} = 35 \pm 4$ mm in the streamwise direction and a width of 115 mm. As the shock impingement is changed from $x_1/a = 0.27$ to 0.42 in Fig. 12(b), the length of the separation region is approximately halved, with the bubble having $L_{sep} = 18 \pm 3$ mm and a width of 111 mm. When the shock moves further downstream, both the length and width of the separation bubble increase slightly. This suggests the existence of a streamwise shock position that results in a separation bubble of minimum size.

Figure 13 shows the effects of changing the shock generator thickness on the topology of the separation region. As the expansion is moved away from the SBLI, the separation length increases. This growth of the separation region occurs via an increase in the SBLI's upstream influence, as the re-attachment point remains approximately the same in all three cases. Both the increase in size of the separation bubble and the invariance in the re-attachment point with increasing SBLI–expansion distances are consistent with the observations of Grossman & Bruce [17] for SBLIs on flat surfaces.

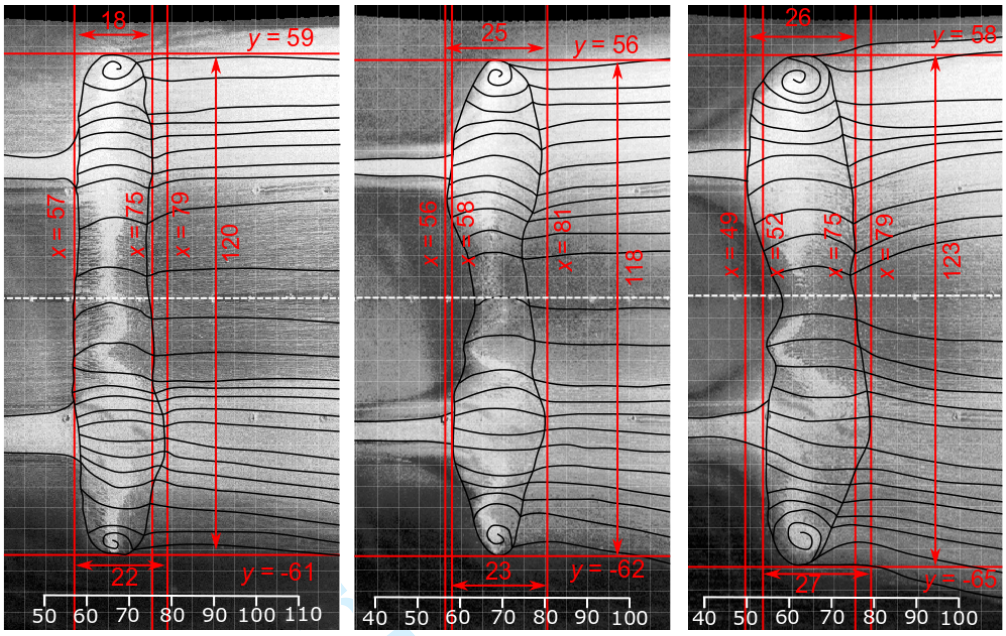

(a) t_{SG} **= 8.0 mm** **(b)** t_{SG} **= 9.5 mm** **(c)** t_{SG} **= 11.3 mm**

Fig. 13 Oil flow visualisation images for different SBLI–expansion distances, at a constant $x_1/a = 0.57$

The separation and re-attachment streamwise locations, x_s and x_r respectively, are tabulated in Table 1 as measured from the oil flow images. These were measured along the streamlines emanating from the oil injection ports, where oil density is greatest. The separation length ~~, defined as $L_{sep} = x_r - x_s$, is also included.~~ (defined as $L_{sep} = x_r - x_s$) and the ratio of the interaction length (as shown in Fig. 7) to the separation length are also included.

Table 1 List of separation and re-attachment points, as measured in the oil flow images.

t_{SG} (mm)	x_1/a	x_s (mm)	x_r (mm)	L_{sep} (mm)	L_{int}/L_{sep}
8.0	0.27	−8 ± 2	26 ± 2	34 ± 4	0.70 ± 0.08
	0.42	40 ± 2	58 ± 1	18 ± 3	1.0 ± 0.2
	0.57	57 ± 1	77 ± 2	20 ± 3	0.7 ± 0.1
	0.72	83 ± 1	104 ± 1	21 ± 2	0.69 ± 0.06
9.5	0.57	57 ± 1	81 ± 1	24 ± 2	0.67 ± 0.06
11.3	0.57	50 ± 2	77 ± 2	27 ± 4	0.7 ± 0.1

E. Numerical simulations

In order to explore the effects of the flexible plate on the downstream total pressure recovery, all the experimental test cases have been reproduced in two-dimensional steady simulations. In these, the experimental spanwise-averaged plate profiles were imposed as solid boundaries. The simplified 2D simulations do not capture some important SBLI effects, such as flow unsteadiness, flow bleeding/injection due to the cavity, and the effect of the sidewall boundary layers. Due to ~~the various assumptions and simplifications made in these~~ these simplifications, some differences between the experimental and simulated flowfields are anticipated. The experimental and numerical results are compared in Sections IV.E.1-3. The calculated stagnation pressure profiles, for which no experimental validation was available, are presented in Section IV.E.4.

1. Flow structures

In order to visualise the computational flowfield, the spatial distribution of some scalar quantity may be considered. Fig. 14 compares a representative Mach number field obtained with the numerical simulations to its corresponding experimental schlieren image.

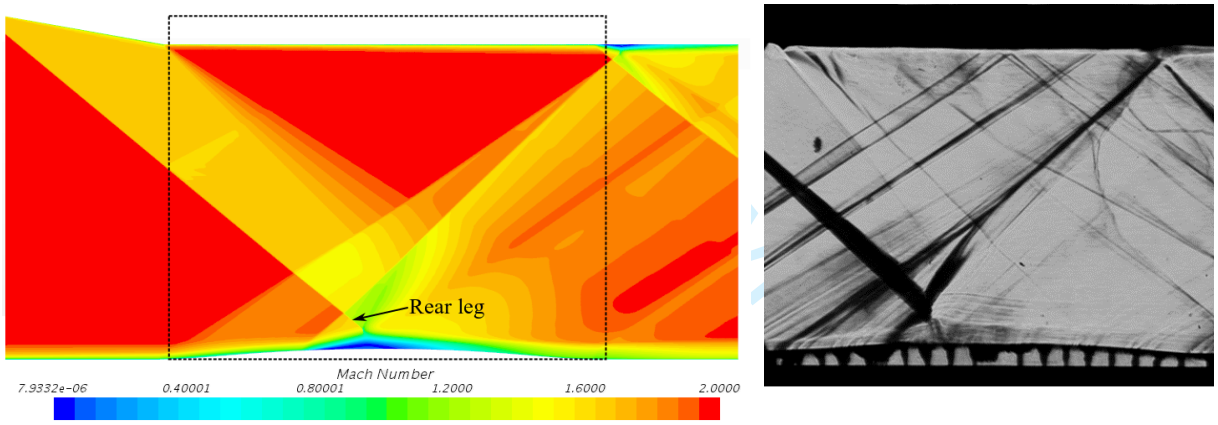

(a) Mach number, CFD **(b) Schlieren, experimental**

Fig. 14 Comparison of the Mach number field obtained with CFD and an experimental schlieren image, both corresponding to the t_{SG} = 11.3 mm, x_1/a = 0.57 test case. The schlieren image in (b) corresponds to the region inside the dashed rectangle in (a).

Figures 14(a) and (b) both show similar flow structures. As shown in 14(a), the numerical simulation predicts the coalescence of the front and induced shocks observed in experiments; however, these shocks intersect further downstream than in 14(b). This is in part due to differences in the induced shock angle, which is visibly shallower in 14(a) than in 14(b). Examining the SBLI itself, the numerical simulations predict a region of supersonic flow outside the separation bubble, as well as a clear SBLI rear leg. In contrast, the schlieren image shows that the flow downstream of the separation shock is highly unsteady, with a barely visible rear leg.

2. Static and Pitot pressure validation

Figure 15 compares the numerical static pressure distributions along the wind tunnel's surface to the experimental ones. In simulations, static pressures in the range $-0.73 \leq x/a \leq 1.33$ are available, but only a part of these are shown in order to ease comparison with the experiments.

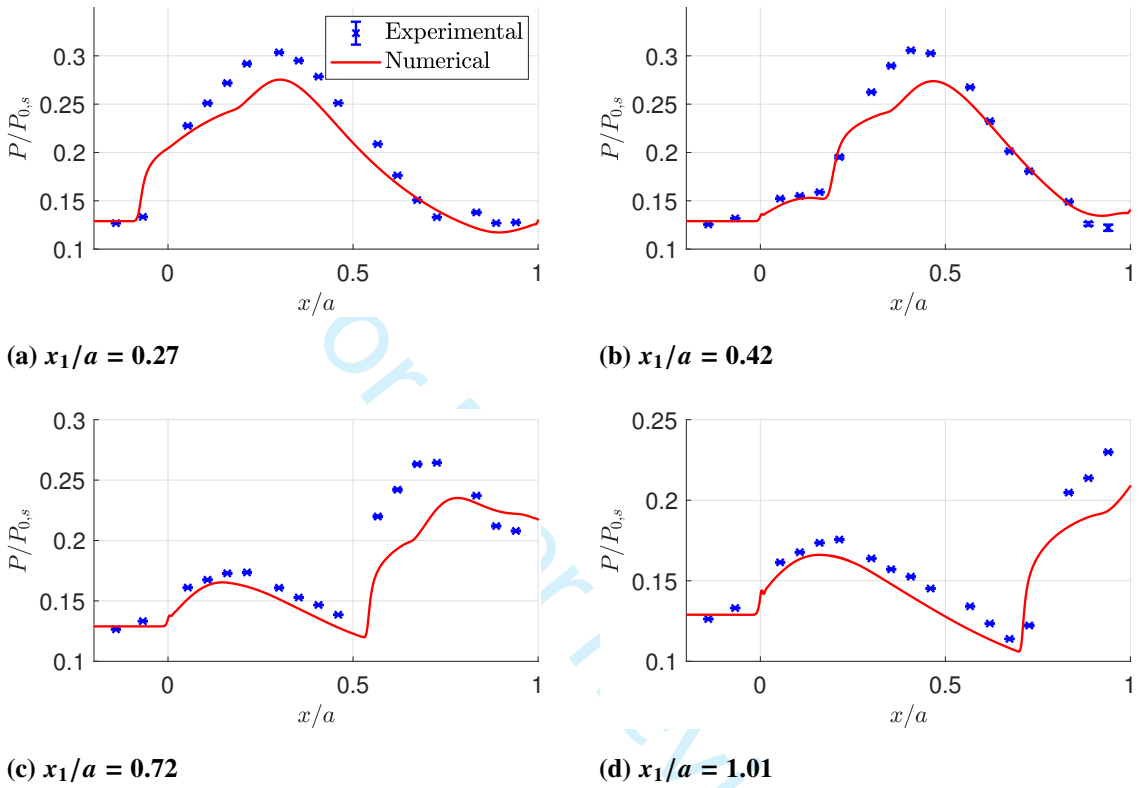

(a) $x_1/a = 0.27$ **(b) $x_1/a = 0.42$**

(c) $x_1/a = 0.72$ **(d) $x_1/a = 1.01$**

Fig. 15 Comparison of the normalized static pressure distributions, obtained with the $t_{SG} = 9.5$ mm shock generator. Error bars represent one standard deviation.

Upstream of the shock, the experimental and CFD pressure profiles agree well. The pressure rises due to plate curvature in Figs. 15(b-d) are very similar in experiments and CFD, with the pressure peak being approximately at the same streamwise location. Nevertheless, the numerical simulations slightly underestimate the pressure magnitude, potentially due to slightly inaccurate interpolated plate curvature, or the inability of the CFD simulations to accurately capture the boundary layer development.

A greater discrepancy between experiments and CFD can be seen after the shock impingement, with numerical simulations consistently underpredicting the magnitude (and hence the strength) of the SBLI pressure rise. ~~Since the SBLI upstream influences are similar in experiments and simulations, this suggests that the CFD simulations are underestimating the outer flow deflection due to the separation bubble.~~ These discrepancies between the experimental and RANS pressure distributions in the SBLI region had been observed in previous studies. As noted by Benek [33], the

computed SBLI pressure rises in RANS simulations relax towards zero pressure gradient faster than in experiments.

All CFD simulations predict a two-step pressure rise due to the SBLI. This has also been observed in other numerical and experimental studies [4, 17]. Nevertheless, this two-step rise is not seen in the experimental pressure distributions. This can be partially attributed to the low spatial resolution of the experimental pressure measurements, which does not allow the complete reconstruction of the SBLI pressure rise. A better agreement between the CFD simulations and the experiments can be seen in the region downstream of the pressure peak (with a favourable pressure gradient) in Figs. 15(a) and (b).

A sensitivity study was conducted to explore the effects of changing the inlet boundary layer thickness (in the range $4 \leq \delta \leq 8$ mm) on the pressure distributions. A slight increase on the upstream influence, and a reduction in the pressure rise, were observed as the boundary layer thickness was increased. However, these changes are small compared to the discrepancies with experiments seen in Fig. 15.

The Rayleigh-Pitot equation, given by Eq. (8.80) in Anderson [32], has been used to calculate the numerical Pitot pressure at a station $x = 180$ mm, which is the location of the Pitot rake in experiments. Figure 16 compares the experimental and numerical Pitot pressures at four different shock impingement locations.

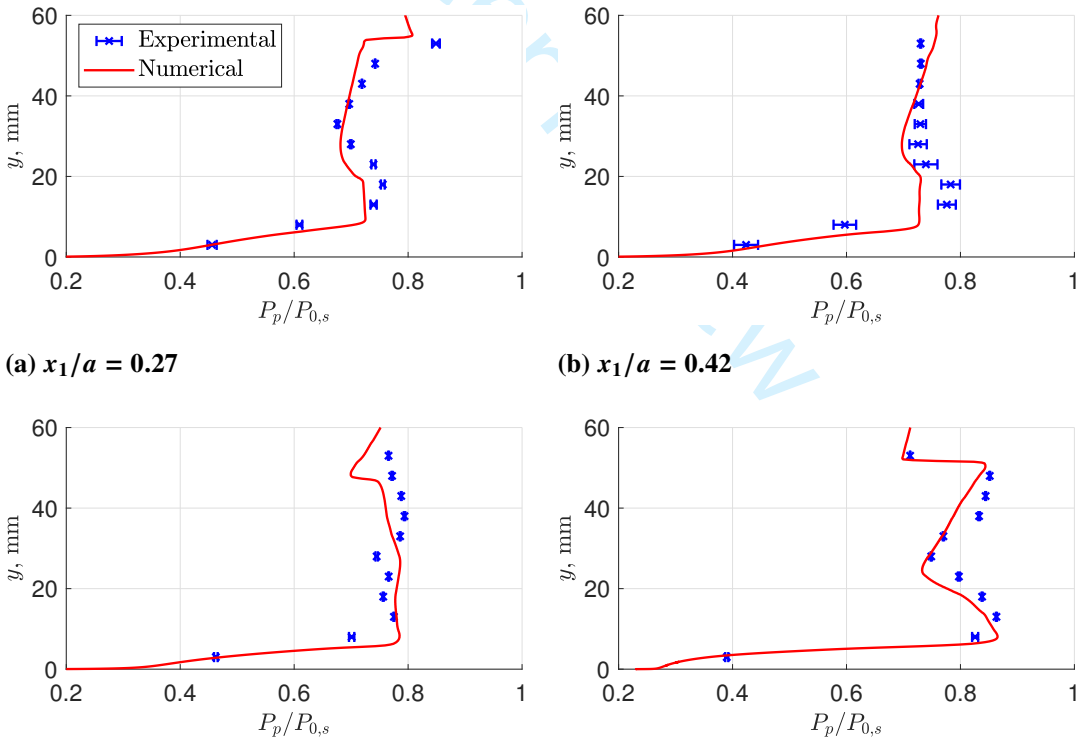

(a) $x_1/a = 0.27$ **(b) $x_1/a = 0.42$**

(c) $x_1/a = 0.72$ **(d) $x_1/a = 1.01$**

Fig. 16 Comparison of the normalized Pitot pressures recorded at $x = 180$ mm from experiments and numerical simulations, obtained with the $t_{SG} = 9.5$ mm shock generator. Error bars represent one standard deviation.

In general, the experimental and numerical Pitot pressure distributions show a good agreement. For example, the numerical simulation in Fig. 16(d) correctly predicts the experimental Pitot pressure profile including the effects of the induced shock, which is responsible for the sudden decrease in the uppermost experimental Pitot measurement. However, CFD slightly underestimates the magnitude of the Pitot pressures in 16(d). The agreement between CFD and experiments is worse in 16(b) and (c). In 16(b), the experimental data displays some unsteadiness, shown by the large error bars, and this is not captured by the steady simulations.

Observing the boundary layer profile, for which only the data points at $y = 3$ mm and $y = 8$ mm are available in experiments, it can be seen that CFD simulations accurately capture the first experimental data point in all four cases, but consistently overpredict the Pitot pressure of the second one, at $y = 8$ mm. ~~This in principle suggests that the post-SBLI experimental boundary layer is thicker than the numerical one; nevertheless, these differences could also be caused by slight inaccuracies in the vertical position of the Pitot probes.~~

3. Separation

A key factor in characterising an SBLI is the separation length. In simulations, the separation (x_s) and re-attachment points (x_r) were inferred from the region where $c_f < 0$. A sample skin-friction plot was shown in Fig. 3. Once these points were known, the separation length was calculated and the results are shown in Fig. 17. Moreover, a set of baseline (reference) values, calculated on a flat surface with different shock generator thicknesses and a shock impinging at $x_1/a = 0.57$, have been added as horizontal lines.

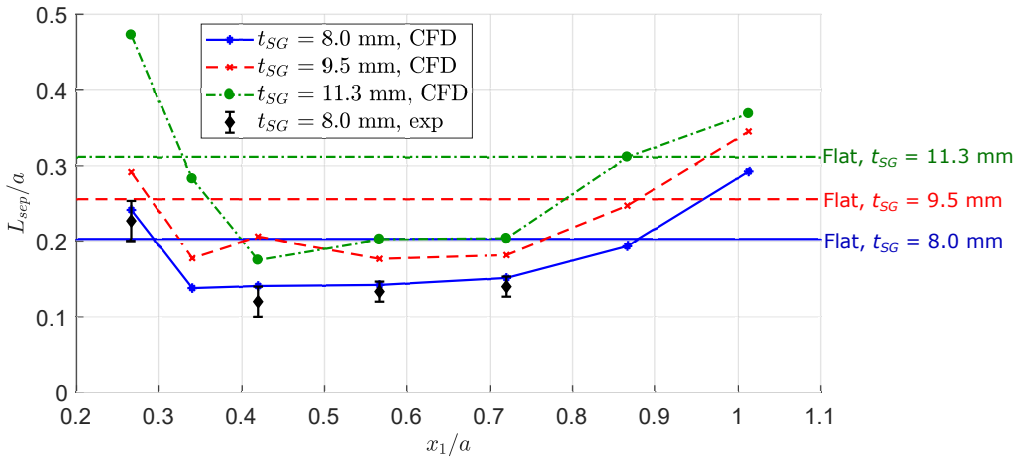

Fig. 17 Variation in separation length with shock impingement position.

Figure 17 shows that, if the shock impinges on the middle region of the bump ($0.34 \leq x_1/a \leq 0.87$), reductions of the order of 40 % in the separation length can be achieved with respect to the flat surface case. This is true for all shock generator thicknesses considered. To validate these predictions, the experimental results obtained with oil flow visualisation are shown superimposed, and these agree well with the CFD values. If the shock impinges too far upstream

or downstream, performance degrades and separation lengths up to 45 % larger than in the flat surface case are observed.

Grossman & Bruce [17] reported that increasing the shock generator thickness resulted in increased separation lengths on a flat surface. As shown in Fig. 17, this is also true when the shock impinges on a deflected surface. Furthermore, even though the flat surface separation lengths have been plotted as horizontal lines (independent of the shock impingement position), in reality, the separation length would be expected to increase slightly as the shock impinges further downstream due to boundary layer thickening.

4. Stagnation pressure

Figure 18 shows the downstream stagnation pressure profiles obtained with the t_{SG} = 9.5 mm shock generator, as predicted by simulations. All stagnation pressures have been calculated at x = 180 mm, as this was the location of the Pitot rake in the experiments.

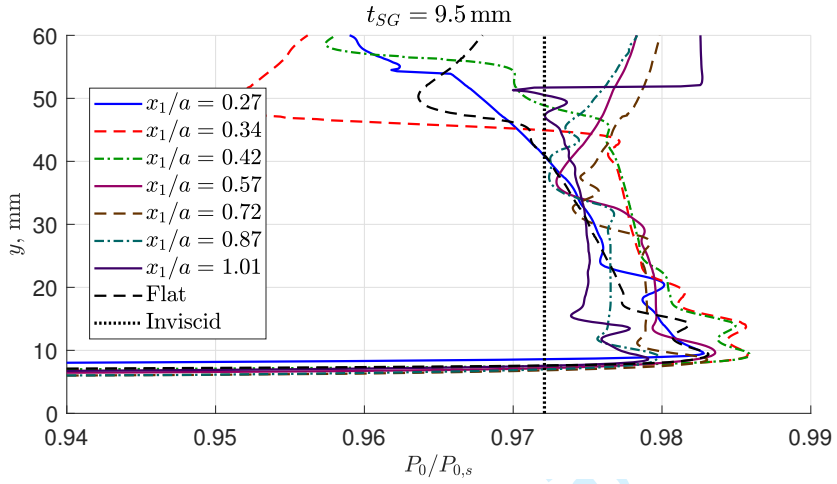

Fig. 18 Stagnation pressure profiles at x = 180 mm for varying shock impingement locations. Only values outside the boundary layer are shown.

Considering first the flow outside the boundary layer (y > 10 mm), it can be seen that the x_1/a = 0.34 and x_1/a = 0.42 shock positions provide the greatest stagnation pressure recovery, at least in the 10 ≤ y ≤ 45 mm region. These are the shock impingement locations that also resulted in the highest peak static pressures in Fig. 8. Nevertheless, these two test cases show a sudden decrease in stagnation pressure for y > 45 mm, and this is caused by the coalescence between the front and induced shocks, as seen in Fig. 5(b).

In order to quantify the effects of the flexible plate on total pressure recovery, a recovery coefficient c_{rec} has been considered. This represents a mass-weighted average of the downstream total pressure, and is defined as

$$c_{rec} = \frac{\int_0^{y_{end}} \rho u \frac{P_0}{P_{0,s}} dy}{\int_0^{y_{end}} \rho u \, dy} \tag{1}$$

where y_{end} is the upper integration limit. Figure 19 shows the calculated recovery coefficient with the three shock generator thicknesses at varying x_1. An upper limit $y_{end} = 53$ mm has been used, as this is the height of the uppermost Pitot probe sampled. In addition, the results obtained on a flat surface with a shock impinging at $x_1/a = 0.57$ have been included as horizontal lines with no markers, ignoring the effects of boundary layer thickening when x_1/a increases.

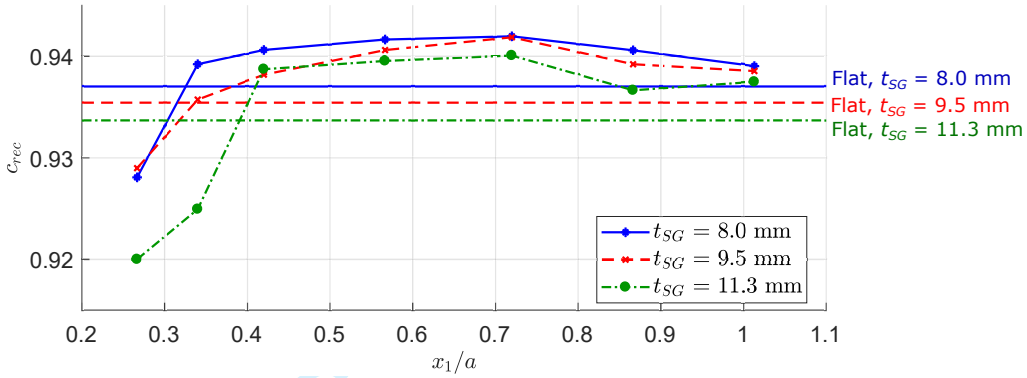

Fig. 19 Mass-weighted stagnation recovery coefficient against shock position.

Improvements in the stagnation pressure recovery are observed with respect to the flat surface case when the shock impinges in the range $0.42 \leq x_1/a \leq 1.01$, with maximum recovery occurring when the shock lies on the central region of the flexible plate ($0.57 \leq x_1/a \leq 0.72$). Reductions between 8% and 10% in the mass-averaged losses are found if this is the case, and this is true for all the SBLI–expansion distances considered.

Examination of the stagnation pressure profiles in Fig. 18 shows that stagnation pressure losses are not dominated by losses in the outer flow, where shock structures play a major role, and rather by dissipation within the boundary layer. Hence, the test cases with thinner boundary layers also provide greater recovery coefficients. In fact, comparison of Figs. 17 and 19 reveals a clear correlation, as the test cases with smaller separation bubbles also provide higher downstream stagnation pressure recovery. It is hypothesized that this is due to reduced viscous dissipation in the separation region.

In order to examine the effects of changing the integration limit y_{end}, a sensitivity study was conducted. This confirmed that the bump can provide improved stagnation pressure recovery irrespective of the integration limits used.

F. Synthesis

The experimental static pressure distributions along the centerline of the plate in Fig. 8 have shown that there exists a shock impingement location that results in maximum pressure on the plate. Tan et al. [6] hypothesized the existence of this optimum point and suggested that it could result in improved stagnation pressure downstream of the bump. Numerical simulations show that this is indeed the case, at least outside the boundary layer, as illustrated in Fig. 18.

Moreover, examining the schlieren and oil flow images for varying shock streamwise impingement positions (Figs. 5

and 12), it was noticed that a shock impinging near the front or rear of the flexible plate caused large separation bubbles and SBLI upstream influences. On the contrary, a shock impinging on some location around the mid-chord of the flexible plate resulted in a separation bubble of minimum length. These observations are further supported by the numerical results in Fig. 17, where this minimum separation length was not only observed, but it was also significantly lower than if the bump were not present. When examining the numerical recovery coefficient in Fig. 19, it was found that, if the shock impinges on the middle of the bump, the flexible surface also provides improved stagnation pressure as compared to the flat surface case. This is due to a combination of reduced separation length (resulting in thinner boundary layers) and more efficient compression of the outer flow.

~~Fig.~~Figure 20 compares the observed flow structures at three different shock impinging positions. If the shock impinges too far upstream, as in Fig. 20(a), or too far downstream, as in 20(c), the large separation bubbles and inefficient flow compression limit the attainable total pressure recovery. The configuration in 20(b) with a shock at the mid-chord provides maximum stagnation pressure recovery. Most importantly, improvements with respect to the flat surface case are found for a range of shock impingement positions: $0.42 \leq x_1/a \leq 1.01$. This suggests that the bump could remain beneficial even for varying flow conditions.

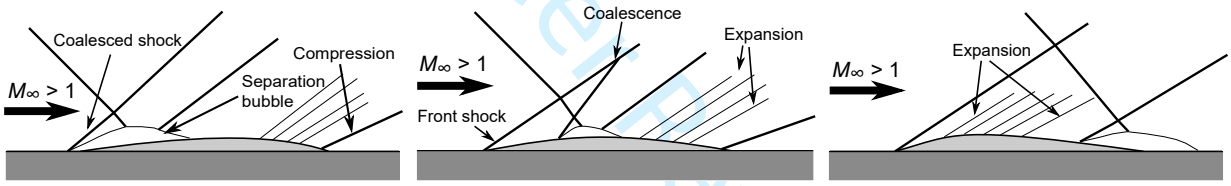

(a) Front impingement **(b) Middle impingement** **(c) Rear impingement**

Fig. 20 Schematic diagrams of SBLIs on a flexible surface at different shock impingement locations. The optimum position for maximum stagnation pressure recovery is shown in (b).

Furthermore, testing with different shock generator thicknesses has shown that these trends of (1) greater static pressure loads, (2) reduced separation length, and (3) improved stagnation recovery if the shock impinges at the mid-chord of the bump are also applicable when the SBLI–expansion distance increases. This highlights the potential application of flexible surfaces for SBLI control in supersonic inlets, where no expansion exists downstream of the shock.

V. Conclusions

This study investigated oblique shock–boundary layer interactions on a flexible panel in an $M_\infty = 2$ flow. A parametric study was conducted in the Imperial College supersonic wind tunnel, in which the effects of varying the shock impingement position and the SBLI–expansion distance were explored. In addition, two-dimensional steady simulations were used to study the effectiveness of the bump in improving downstream total pressure recovery. The computational

results were validated against static and Pitot pressure experimental measurements. Numerical simulations accurately predict the main trends in the static and Pitot pressure profiles, although they consistently underpredict the SBLI pressure rise.

By moving the shock generator in the streamwise direction, inviscid shock impingement positions in the range $0.27 \leq x_1/a \leq 1.01$ have been tested. The static pressure distributions, measured along the centerline of the flexible surface, have shown that maximum static pressure is achieved when the shock impinges on the region $0.34 \leq x_1/a \leq 0.57$, with the exact location varying depending on the shock generator thickness. This maximum exists because of the combined flow compression due to plate curvature and the SBLI, before any flow re-acceleration.

Oil flow visualization was used to measure the separation length. Numerical simulations, which agree well with the experimental values, show reductions of the order of 40 % in the separation length with respect to the flat surface case if the shock impinges on the flexible plate in the range $0.34 \leq x_1/a \leq 0.87$. When the SBLI lies outside this range, a degradation in performance is observed, resulting in separation lengths up to 45 % larger than if the flexible surface were not used.

Using numerical simulations, improvements in downstream stagnation pressure recovery with respect to the flat surface case are also found for shock positions in the range $0.42 \leq x_1/a \leq 1.01$. In particular, CFD results show that the mass-averaged stagnation pressure losses can be reduced by between 8 % and 10 % if a flexible surface is used.

The effects of changing the SBLI–expansion were explored by varying the shock generator thickness between $t_{SG} = 11.3$ and 8.0 mm, while maintaining a constant tunnel aspect ratio $\mathcal{AR} = 1.25$. Experimental results show reductions in the static pressure rise when the expansion is moved closer to the SBLI, implying a weakening of the interaction. Similarly, decreasing the SBLI–expansion distance also results in a reduction in the SBLI upstream influence, as shown by schlieren images and static pressure distributions. Both oil flow and computational results show that this decrease in the upstream influence is associated with a reduction in size of the separation bubble. Furthermore, the improvements in separation length and total pressure recovery when the shock impinges on the middle of the bump were found to occur for all the shock generator thicknesses used in the simulations.

Further research is desirable to confirm whether the beneficial performance of flexible surfaces for oblique shock control holds across a wider range of shock angles and Mach numbers. Such tests would be necessary to verify the considerable potential of flexible surfaces as a passive and mechanically-simple form of shock control in next-generation supersonic inlets.

Acknowledgments

The second author would like to acknowledge the Imperial College President's PhD Scholarship Scheme, supported by EPSRC, for their support of this research. The authors wish to acknowledge Mr Dilaksan Thillaithevan for his assistance with the experimental testing.

References

[1] Hirt, S., Reich, D., and O'Connor, M., "Microramp Flow Control for Oblique Shock Interactions: Comparisons of Computational and Experimental Data," *5th Flow Control Conference*, American Institute of Aeronautics and Astronautics, 2010. doi: https://doi.org/10.2514/6.2010-4973.

[2] Giepman, R. H. M., Schrijer, F. F. J., and van Oudheusden, B. W., "Flow control of an oblique shock wave reflection with micro-ramp vortex generators: Effects of location and size," *Physics of Fluids*, Vol. 26, No. 6, 2014, p. 066101. doi:https://doi.org/10.1063/1.4881941.

[3] Zhang, Y., jun Tan, H., Sun, S., and yan Rao, C., "Control of Cowl Shock/Boundary-Layer Interaction in Hypersonic Inlets by Bump," *AIAA Journal*, Vol. 53, No. 11, 2015, pp. 3492–3496. doi:https://doi.org/10.2514/1.j053974.

[4] Brouwer, K. R., Gogulapati, A., and McNamara, J. J., "Interplay of Surface Deformation and Shock-Induced Separation in Shock/Boundary-Layer Interactions," *AIAA Journal*, Vol. 55, No. 12, 2017, pp. 4258–4273. doi:https://doi.org/10.2514/1.j056030.

[5] Zhang, Y., Tan, H.-J., Li, J.-F., and Yin, N., "Control of Cowl-Shock/Boundary-Layer Interactions by Deformable Shape-Memory Alloy Bump," *AIAA Journal*, 2018, pp. 1–10. doi:https://doi.org/10.2514/1.j057409.

[6] Tan, S. S., Bruce, P. J. K., and Gramola, M., "Oblique Shockwave Boundary Layer Interaction on a Flexible Surface," *AIAA Scitech 2019 Forum*, American Institute of Aeronautics and Astronautics, 2019. doi:https://doi.org/10.2514/6.2019-0097.

[7] Ashill, P. R., Fulker, J. L., and Shires, A., "A novel technique for controlling shock strength of laminar-flow aerofoil sections," *DGLR Bericht Part 6*, Vol. (92–01–022), 1992, pp. 175–183.

[8] Birkemeyer, J., Rosemann, H., and Stanewsky, E., "Shock control on a swept wing," *Aerospace Science and Technology*, Vol. 4, No. 3, 2000, pp. 147–156. doi:https://doi.org/10.1016/s1270-9638(00)00128-0.

[9] Bruce, P. J. K., Colliss, S., and Babinsky, H., "Three-dimensional shock control bumps: effects of geometry," *52nd Aerospace Sciences Meeting*, American Institute of Aeronautics and Astronautics, 2014. doi:https://doi.org/10.2514/6.2014-0943.

[10] Kim, S. D., "Aerodynamic Design of a Supersonic Inlet with a Parametric Bump," *Journal of Aircraft*, Vol. 46, No. 1, 2009, pp. 198–202. doi:https://doi.org/10.2514/1.37416.

[11] Bruce, P. J. K., and Colliss, S. P., "Review of research into shock control bumps," *Shock Waves*, Vol. 25, No. 5, 2014, pp. 451–471. doi:https://doi.org/10.1007/s00193-014-0533-4.

[12] Ogawa, H., Babinsky, H., Pätzold, M., and Lutz, T., "Shock-Wave/Boundary-Layer Interaction Control Using Three-Dimensional Bumps for Transonic Wings," *AIAA Journal*, Vol. 46, No. 6, 2008, pp. 1442–1452. doi:https://doi.org/10.2514/1.32049.

[13] Visbal, M., "Viscous and inviscid interactions of an oblique shock with a flexible panel," *Journal of Fluids and Structures*, Vol. 48, 2014, pp. 27–45. doi:https://doi.org/10.1016/j.jfluidstructs.2014.02.003.

[14] Jinks, E. R., Bruce, P. J. K., and Santer, M. J., "The Use of Actuated Flexible Plates for Adaptive Shock Control Bumps," *53rd AIAA Aerospace Sciences Meeting*, American Institute of Aeronautics and Astronautics, 2015. doi:https://doi.org/10.2514/6.2015-1241.

[15] Gramola, M., Bruce, P. J. K., and Santer, M. J., "FSI study of 2D adaptive shock control bumps," *AIAA Scitech 2019 Forum*, American Institute of Aeronautics and Astronautics, 2019. doi:https://doi.org/10.2514/6.2019-1845.

[16] Shinde, V., Gaitonde, D. V., and McNamara, J. J., "Control of Transitional Shock Boundary Layer Interaction using Surface Morphing," *AIAA Scitech 2019 Forum*, American Institute of Aeronautics and Astronautics, 2019. doi:https://doi.org/10.2514/6.2019-1895.

[17] Grossman, I. J., and Bruce, P. J. K., "Effect of Test Article Geometry on Shock Wave-Boundary Layer Interactions in Rectangular Intakes," *55th AIAA Aerospace Sciences Meeting*, American Institute of Aeronautics and Astronautics, 2017. doi:https://doi.org/10.2514/6.2017-0758.

[18] Hirt, S. M., "Experimental Study of Fillets to Reduce Corner Effects in an Oblique Shock-Wave/Boundary-Layer Interaction," *53rd AIAA Aerospace Sciences Meeting*, American Institute of Aeronautics and Astronautics, 2015. doi:https://doi.org/10.2514/6.2015-1239.

[19] Grossman, I. J., and Bruce, P. J. K., "Effect of Confinement on Shock Wave-Boundary Layer Interactions in Rectangular intakes," *54th AIAA Aerospace Sciences Meeting*, American Institute of Aeronautics and Astronautics, 2016. doi:https://doi.org/10.2514/6.2016-0348.

[20] Threadgill, J. A., and Bruce, P. J. K., "Unsteadiness in Shock Wave Boundary Layer Interactions across Multiple Interaction Configurations," *53rd AIAA Aerospace Sciences Meeting*, American Institute of Aeronautics and Astronautics, 2015. doi:https://doi.org/10.2514/6.2015-1977.

[21] Jinks, E. R., Bruce, P. J. K., and Santer, M. J., "Wind Tunnel Experiments with Flexible Plates in Transonic Flows," *54th AIAA Aerospace Sciences Meeting*, American Institute of Aeronautics and Astronautics, 2016. doi:https://doi.org/10.2514/6.2016-1553.

[22] Dowell, E. H., "Panel flutter - A review of the aeroelastic stability of plates and shells," *AIAA Journal*, Vol. 8, No. 3, 1970, pp. 385–399. doi:https://doi.org/10.2514/3.5680.

[23] Gramola, M., Bruce, P. J. K., and Santer, M., "Photogrammetry for accurate model deformation measurement in a supersonic wind tunnel," *Experiments in Fluids*, Vol. 60, No. 1, 2018. doi:https://doi.org/10.1007/s00348-018-2652-7.

[24] *PhotoModeler Motion*, PhotoModeler Technologies, 2019.

[25] Stamatopoulos, N., Gatos, B., Pratikakis, I., and Perantonis, S. J., "A Two-Step Dewarping of Camera Document Images," *2008 The Eighth IAPR International Workshop on Document Analysis Systems*, IEEE, 2008. doi:https://doi.org/10.1109/das.2008.40.

[26] Babinsky, H., Oorebeek, J., and Cottingham, T., "Corner effects in reflecting oblique shock-wave/boundary-layer interactions," *51st AIAA Aerospace Sciences Meeting including the New Horizons Forum and Aerospace Exposition*, American Institute of Aeronautics and Astronautics, 2013. doi:https://doi.org/10.2514/6.2013-859.

[27] Bruce, P. J. K., Burton, D. M. F., Titchener, N. A., and Babinsky, H., "Corner effect and separation in transonic channel flows," *Journal of Fluid Mechanics*, Vol. 679, 2011, pp. 247–262. doi:https://doi.org/10.1017/jfm.2011.135.

[28] *Star-CCM+*, Siemens PLM Software, 2018. Version 13.04.011.

[29] Singh, A. P., Duraisamy, K., and Pan, S., "Characterizing and Improving Predictive Accuracy in Shock-Turbulent Boundary Layer Interactions Using Data-driven Models," *55th AIAA Aerospace Sciences Meeting*, American Institute of Aeronautics and Astronautics, 2017. doi:https://doi.org/10.2514/6.2017-0314.

[30] Bardina, J. E., Huang, P. G., and Coakley, T. J., "Turbulence modeling validation, testing, and development," NASA Technical Memorandum 110446, NASA, 1997.

[31] Schlichting, H., and Gersten, K., *Boundary-Layer Theory*, Springer-Verlag GmbH, 2016.

[32] Anderson, J. D., *Fundamentals of Aerodynamics*, 5th ed., McGraw-Hill Education Ltd, 2010.

[33] Benek, J., "Lessons Learned from the 2010 AIAA Shock Boundary Layer Interaction Prediction Workshop," *28th AIAA Applied Aerodynamics Conference*, American Institute of Aeronautics and Astronautics, 2010. doi:https://doi.org/10.2514/6.2010-4825.

Oblique shock control with steady flexible panels

Supplemental materials

1 Plate design

The plate assembly contains a thin panel of length $a = 150\,\text{mm}$, width 149 mm, and thickness $h = 0.6\,\text{mm}$. The assembly also includes two thicker structural supports to which the plate is attached. These supports are bolted to the bottom of the wind tunnel at four points each. Two holes were drilled into the downstream support to accommodate a rake of Pitot probes and their corresponding connections. The two longitudinal ends of the flexible plate are clamped to the supports, while the two sides are free. The entire assembly is made of aluminum alloy Al 7075-T6. A schematic diagram of the plate assembly is shown in Figure 1. The figure shows that two bars are attached to the flexible portion of the plate, and these are actuator supports that have been used in previous experiments. However, the plate was not actuated in this study.

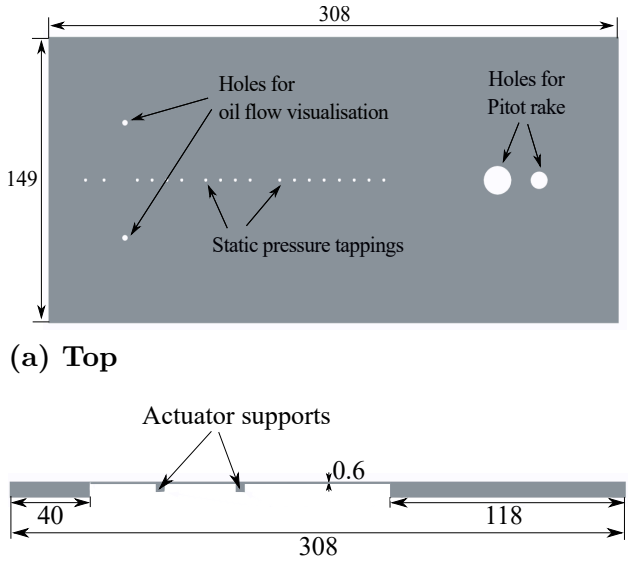

(a) Top

(b) Front

Figure 1: Schematic diagram of the plate assembly. Dimensions in mm.

2 Cavity pressure

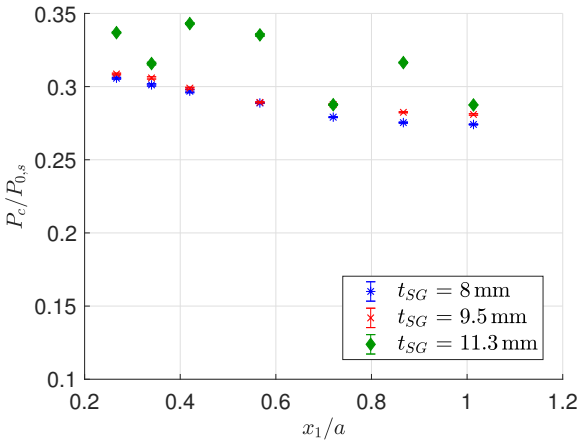

Figure 2: Normalized cavity pressure recorded during each test case. Error bars represent one standard deviation.

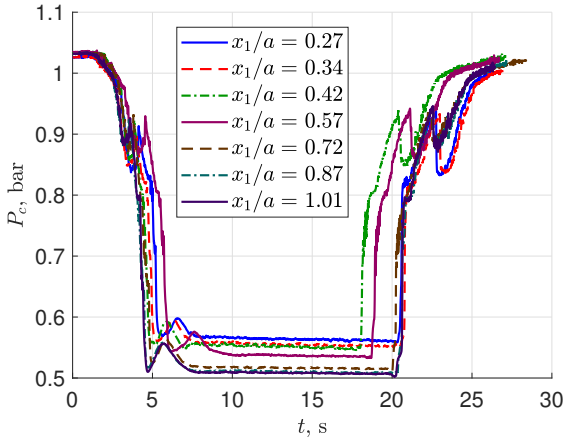

Figure 3: Time history of the cavity pressure during the $t_{SG} = 8.0\,\text{mm}$ runs

Since the pressure difference between the flow and the cavity is the main driver of plate deformations, pressure in the cavity was recorded. The average cavity pressure measured in each experiment is shown in Figure 2. In order to ease comparison

with Figs. 8 and 9 in the text, the same y-scale is used. The differences in cavity pressure when the shock generator thickness is changed are attributed to the different flow conditions in the test section, to which the cavity is connected. These pressures were recorded once the starting shock had been swallowed and the tunnel was fully started.

The time history of the cavity pressure during wind tunnel runs is shown in Figure 3 for the $t_{SG} = 8.0\,\text{mm}$ cases. The figure shows a region of steady low pressure, when the tunnel was fully started and pressure measurements were taken.

3 Integrated pressure loads

Panel deformations are driven by the pressure difference between the upper and lower side of the panel. The pressure loads shown in Fig. 8 in the main text and Figure 2 in this document were integrated in the streamwise direction using the trapezoidal method to obtain the total pressure force on the panel. The results are shown in Figure 4, for (a) the upper pressure loading only, and (b) the pressure difference between the cavity and the flow, $\Delta P = P_c - P$. The results in Figure 4(b) show large dispersion for varying shock position and shock generator thickness, as a result of the sensitivity of cavity pressure to flow conditions. The cavity pressure affects the static pressure on the upper side of the panel via plate deformations. The results show that the relatively large dispersion of the data in Figure 4(b) is not reflected on the upper surface pressure loading in Figure 4(a).

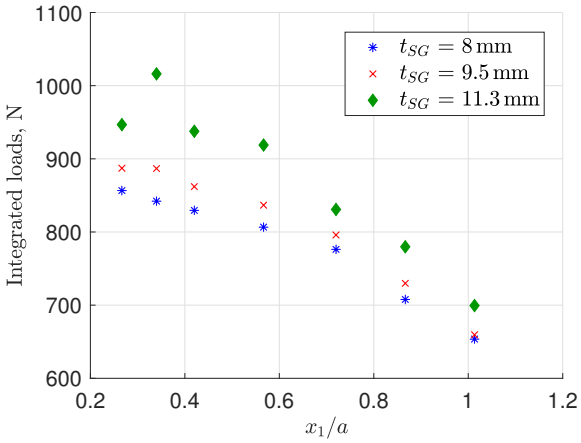

(a) Pressure on upper side only

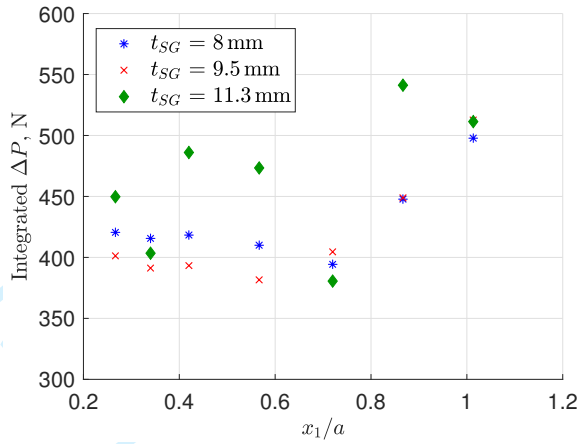

(b) Pressure difference

Figure 4: Integrated pressure force on the flexible plate for each test case